Resolution enhancement of SMOS brightness temperatures: application to melt detection on the Antarctic and Greenland ice sheets

Pierre Zeiger, Ghislain Picard, Philippe Richaume, Arnaud Mialon, Nemesio Rodriguez-Fernandez

Resolution enhancement of SMOS brightness temperatures: application to melt detection on the Antarctic and Greenland ice sheets

Pierre Zeiger[a,*], Ghislain Picard[a], Philippe Richaume[b], Arnaud Mialon[b], Nemesio Rodriguez-Fernandez[b]

[a] *Institut des Géosciences de l'Environnement (IGE), CNRS/UGA, Grenoble, France*
[b] *Centre d'Etudes Spatiales de la Biosphère (CESBIO), CNES, Toulouse, France*

Abstract

A large part of the surface of the Greenland Ice Sheet (GrIS) and the margins of Antarctica are melting every summer, affecting their surface mass balance. Wet/dry snow status has been detected for decades using the peaks of brightness temperature at 19 GHz, and more recently at L-band (1.4 GHz) using both the SMOS and SMAP missions. SMOS owns a longer time series than SMAP with data since 2010, but the 52.5° incidence bin in the Level 3 (L3) product from Centre Aval de Traitement des Données SMOS (CATDS) that was previously used to detect melt suffers from a coarse spatial resolution. For this reason, we developed a new SMOS enhanced resolution brightness temperature (T_B) product building on the radiometer version of the Scatterometter Image Reconstruction (rSIR) algorithm. We also exploited the SMOS L1C observations near 40° incidence angle instead of 52.5° as the native spatial resolution of SMOS is better at low incidence. The new product is posted on a 12.5 km polar stereographic grid and covers all the GrIS and Antarctica for 2010-2024 with twice-daily morning and afternoon acquisitions. The effective spatial resolution was evaluated to ∼30 km, a 30 % enhancement compared to the SMOS L3TB at 40° and almost a 50 % enhancement compared to the SMOS L3TB at 52.5°. Then, we applied a melt detection algorithm to both the enhanced resolution product at 40° and the L3TB product at 52.5° which is used in the literature. The spatial resolution enhancement results not only in the detection of smaller melt regions but also in a widespread increase in the annual number of melt days. This increase is larger than 30 days per year in the GrIS percolation area and on multiple Antarctic ice shelves. This is primarily due to the mix of dry and wet snow regions near the ice shelves grounding line, resulting in lower brightness temperature peaks in the SMOS L3TB product due to a large power spread. These findings highlight the dependence of melt detection in particular, and geophysical applications in general, on the spatial resolution of passive microwave observations. This study provides a new open dataset suitable to monitor melt at the surface and at depth on the two main ice-sheets.

Keywords: SMOS, melt, Antarctica, Greenland, resolution enhancement, rSIR

1. Introduction

Surface melt occurs each summer over a large part of the Greenland Ice Sheet (GrIS) and over the margins of the Antarctic Ice Sheet (AIS) (Picard & Fily, 2006; Mote, 2007). It contributes to the ice sheet mass balance both directly through the reduction of surface mass balance (SMB) and indirectly through the enhancement of ice

*Corresponding author

dynamics (Otosaka et al., 2023). Over the GrIS, the widespread surface melt in summer drives the negative SMB accounting for 34% to 50% of the total mass loss (Mouginot et al., 2019; IMBIE, 2020), with an increasing trend in meltwater runoff since the 1990s (Fettweis et al., 2017; IMBIE, 2020). On the contrary, the colder and drier AIS experiences melt only over the margins and the mass loss primarily comes from ice dynamics (IMBIE, 2018; Rignot et al., 2019). Most of the meltwater produced in the AIS percolates in the snowpack or forms ponds at the surface of ice shelves (Kingslake et al., 2017; Stokes et al., 2019), while runoff to the ocean is very low. When refreezing, meltwater creates impermeable ice layers which foster again the formation of supraglacial lakes. Melt ponds play a role in hydrofracturing, potentially leading to the destabilization of ice shelves (Scambos et al., 2000), and are known to have triggered the collapses of the Larsen A and B ice shelves in 1995 and 2002 (Rott et al., 1996; Scambos et al., 2004; Banwell et al., 2013) and of the Wilkins ice shelf in 2008 (Scambos et al., 2009). An important consequence is the acceleration of outlet glaciers that are not anymore buttressed by their downstream ice shelves (Rott et al., 2002; Scambos et al., 2004). The monitoring of surface melt and liquid water percolation is therefore essential to understand and predict runoff and ice dynamics on the ice sheets.

Remote sensing is a suitable tool for detecting the presence of liquid water in the snowpack at large scale. Microwave radiometers have provided a near twice-daily coverage of polar regions since 1988 and every other days since 1979, combining the Scanning Multichannel Microwave Radiometer (SMMR), Special Sensor Microwave Imager (SSM/I), Special Sensor Microwave Imager Sounder (SSMIS) and Advanced Microwave Scanning Radiometer (AMSR-E and AMSR2) sensors. The time series of 19 GHz and 37 GHz brightness temperatures (T_B) were used to detect wet snow occurrence and compute trends and anomalies for up to four decades (Zwally & Fiegles, 1994; Abdalati & Steffen, 1995; Torinesi et al., 2003; Liu et al., 2006; Picard & Fily, 2006; Picard et al., 2007; Tedesco, 2007; Tedesco & Fettweis, 2020). Active microwave sensors are also suitable for wet snow detection, with Synthetic Aperture Radars (SAR) such as Sentinel-1 at C-band (Liang et al., 2021), and scatterometters such as the Quik Scatterometter (QuikSCAT) at Ku-band (Ashcraft & Long, 2006; Trusel et al., 2012) and the Advanced Scatterometter (ASCAT) at C-band (Bevan et al., 2018; Kuipers Munneke et al., 2018). Lastly, optical sensors can detect the accumulation of meltwater at the surface when it forms slush, ponds and streams (Yang & Smith, 2013; Bell et al., 2017; Williamson et al., 2018; Banwell et al., 2019).

The difference between the imaginary part of the permittivity of ice and water (related to absorption) is responsible for a large increase in the T_B at any microwave frequency when liquid water appears in snow (Zwally, 1977; Picard et al., 2022). Multiple algorithms have been proposed in the past 30 years for detecting melt using microwave radiometers, with most of them being based on simple thresholding methods (Zwally & Fiegles, 1994; Abdalati & Steffen, 1995; Ramage & Isacks, 2002; Torinesi et al., 2003; Picard & Fily, 2006; Tedesco, 2007). All these algorithms use the 19 GHz and 37 GHz signals to detect liquid water in the first meter of the snowpack (Picard et al., 2022). However, lower frequencies (e.g. L-band) can provide additional insights on the presence of meltwater at great depths (Colliander et al., 2022, 2023).

The European Space Agency (ESA) Soil Moisture and Ocean Salinity (SMOS, Kerr et al. (2001)) and the Na-

tional Aeronautics and Space Administration (NASA) Soil Moisture Active and Passive (SMAP, Entekhabi et al. (2010)) satellites have provided T_B at L-band (1.4 GHz) since 2010 and 2015, respectively. Both have been recently used to detect melt (Leduc-Leballeur et al., 2020; Mousavi et al., 2022) and can be used in synergy with higher frequency sensors such as SSMIS or AMSR2 (Colliander et al., 2022, 2023). Both sensors are mostly limited by a coarse instrumental spatial resolution. For SMOS, the spatial resolution varies within the field of view from $\sim$30 km to $\sim$60 km depending on the incidence angle, with an average resolution of 43 km (Kerr et al., 2010). SMAP antenna achieves a comparable resolution with an instantaneous field of view of 39 km $\times$ 47 km (Piepmeier et al., 2017). For both sensors, the resolution of conventional gridded T_B products is slightly worse than the instrumental resolution due to the averaging of multiple observations with varying geometry in one pixel (Al Bitar et al., 2017; Long et al., 2023). The coarse spatial resolution of these products is therefore not sufficient to capture small-scale melt patterns observed for instance on the Shackleton (Saunderson et al., 2022) and Larsen C (Luckman et al., 2014) ice shelves. The melt detection algorithm for SMOS presented in Leduc-Leballeur et al. (2020) is indeed based on the SMOS Level 3 T_B (L3TB) product at 52.5° incidence angle with a 25 km grid sampling, but its effective spatial resolution is coarser than 50 km. As a consequence, it is necessary to assess whether the detected melt is resolution-dependent or not, *i.e.*, whether an improvement in spatial resolution leads to an increase of the melt signal detected by SMOS. For this purpose, a SMOS enhanced resolution gridded T_B dataset needs to be first developed.

The reconstruction of radiometer images with enhanced resolution exploits the overlap of multiple observations before their averaging into gridded products. It has been mostly performed using two algorithms: the Backus-Gilbert (BG) inversion technique (Backus & Gilbert, 1967, 1968; Stogryn, 1978), and the radiometer version of the Scatterometer Image Reconstruction (rSIR) algorithm (Long & Daum, 1998). None of these algorithms have been previously applied to interferometric radiometers like SMOS. For conventional radiometers, the previous works from Long & Daum (1998) and Long & Brodzik (2016) indicated that the BG and rSIR algorithms produce output images with an equivalent resolution. However, both the noise and the computation time are significantly higher using BG compared to rSIR. Based on these evaluations, they have been using rSIR to produce enhanced resolution brightness temperature datasets for SSM/I, AMSR-E (Long & Brodzik, 2016) and SMAP (Long et al., 2019).

This study presents the first resolution enhancement of SMOS brightness temperatures and its application to detect melt on the Antarctic and Greenland Ice Sheets. Given the large amount of SMOS data to process, computation time is critical. For this reason, we applied the rSIR algorithm rather than BG to the SMOS Level 1C (L1C) data. Furthermore, we have taken advantage of SMOS multi-incidence capabilities to reconstruct three distinct products. The first one is the *Single-incidence Enhanced Resolution* dataset at 52.5° ($SiER_{52.5}$), and uses the measurements in the 50° - 55° incidence bin to compare with the L3TB at 52.5°. The second one is a similar dataset computed using the 37.5° - 42.5° incidence bin ($SiER_{40}$), at SMAP looking angle, where the native spatial resolution of SMOS observations is better. The third dataset, called *Multi-incidence Enhanced Resolution*

(MiER), uses all the measurements with an incidence angle lower than 40° to exploit the observations with the best native spatial resolution near nadir. For each of these new datasets, we first evaluated the effective spatial resolution and then we applied the melt detection algorithm from Leduc-Leballeur et al. (2020). Comparisons are performed against the L3 T_{B} and melt products to highlight the major changes due to spatial resolution enhancement.

Section 2 presents the different datasets used as input and for validation, Section 3 presents the whole methodology, Section 4 presents the results for the spatial resolution improvement and melt detection, and finally Section 5 discusses the limitations and perspectives to this work.

2. Data

2.1. SMOS Level 1C product

The Microwave Imaging Radiometer using Aperture Synthesis (MIRAS) instrument onboard SMOS is an interferometric radiometer operating at 1.4 GHz (Kerr et al., 2010). It is composed of 69 Lightweight Cost-Effective Front-end (LICEF) receivers which are equally distributed over a central structure and three deployable arms. The signal acquired by each LICEF receiver for one SMOS snapshot is transmitted to a central processing unit that performs cross-correlation to deliver the observables. In full polarization mode, MIRAS furnishes co- and cross-polarized T_{B} in the XY antenna frame with a 1.2 s integration time (Wu et al., 2013). Co-polarized snapshots provide real $T_{\mathrm{B}}^{\mathrm{XX}}$ or $T_{\mathrm{B}}^{\mathrm{YY}}$ measurements while cross-polarized snapshots provide complex measurements T_B^{XY} = $Re(T_{\mathrm{B}}^{\mathrm{XY}})$ + $Im(T_{\mathrm{B}}^{\mathrm{XY}})$. All the values of $T_{\mathrm{B}}^{\mathrm{XX}}$, $T_{\mathrm{B}}^{\mathrm{YY}}$, $Re(T_{\mathrm{B}}^{\mathrm{XY}})$ and $Im(T_{\mathrm{B}}^{\mathrm{XY}})$ are estimated at fixed positions sampled every $\sim$15 km in the equal-area Discrete Global Grid (DGG, Sahr et al. (2003)). Hereafter, a DGG refers to the location of these low-level SMOS measurements.

The SMOS L1C T_{B}, version 724 distributed by ESA is the single input our processing chain requires. The L1C data are distributed by half orbit, 29 per day (both ascending and descending). L1C data blocks include the $T_{\mathrm{B}}^{\mathrm{XX}}$, $T_{\mathrm{B}}^{\mathrm{YY}}$, $Re(T_{\mathrm{B}}^{\mathrm{XY}})$ and $Im(T_{\mathrm{B}}^{\mathrm{XY}})$ acquired by MIRAS in full-polarization mode along with the longitude, latitude, altitude and identifier of each DGG, the radiometric accuracy (RA), azimuth and incidence angles, the semi-minor and semi-major axes of an ellipse approximating the -3 dB footprint of a measurement, and L1C flags which are further used in Section 3.1. For the purpose of this study, we downloaded all the L1C files from April 2010 to March 2024 and we extracted the Antarctic and Greenland measurements for each track.

2.2. SMOS CATDS Level 3 Brightness Temperatures

The Centre Aval de Traitement des Données SMOS (CATDS) produces twice-daily, horizontal and vertical-polarized T_{B} maps from SMOS posted on the EASE-2 Grid at 25 km, for each 5° incidence angle bin ranging from 0° to 65° (Al Bitar et al., 2017). The SMOS L3TB product is obtained by averaging the L1C T_{B} in all the grid pixels for each incidence bin. The averaging of multiple measurements with varying footprints and independent noise results in both a lower spatial resolution and a lower radiometric noise than the L1C T_{B}. SMOS L3TB

has been used in cryospheric studies in particular using the near-Brewster angle (50-55°) (Macelloni et al., 2019; Leduc-Leballeur et al., 2020; Houtz et al., 2021). In this study, the L3TB version 331 at bins 50-55° and 37.5-42.5° are merged on a daily basis to compare with the outputs of our processing chain (Section 3).

2.3. SMAP rSIR-Enhanced Brightness Temperatures

For the purpose of comparison with our new products, and especially for assessing the effective spatial resolution, we used the SMAP Radiometer Twice-Daily rSIR-Enhanced EASE-Grid 2.0 Brightness Temperatures Version 2 dataset (Long et al., 2019; Brodzik et al., 2021) distributed at the National Snow and Ice Data Center (NSIDC). This product contains morning and evening SMAP T_{B} posted on EASE-2 grids with a pixel spacing of 3 km, 3.125 km, 9 km, 25 km, and 36 km. The resolution of SMAP instrument is still unchanged ($\sim$40 km) for all these datasets. The resolution enhancement is based on the same rSIR algorithm that we used in this study for SMOS and that was previously applied to SSM/I, SSMIS and AMSR data (Long & Daum, 1998; Long & Brodzik, 2016). Only the number of iterations differs. We downloaded the SMAP rSIR-enhanced, Version 2 3.125 km T_{B} maps for two particular events lasting three days each where the spatial resolution is evaluated (Section 3.4). A single 12.5 km SMOS L1C rSIR-enhanced pixel therefore contains 16 SMAP rSIR-enhanced pixels.

2.4. Sentinel-1 images

We used images from the ESA Sentinel-1 SAR Ground Range Detected (GRD) product in the process of quantifying the effective spatial resolution of the SMOS enhanced-resolution maps. Two sets of images were chosen: the first one is over Anvers Island (-64.5° latitude, -63.5° longitude) in the Antarctic Peninsula (AP) on the 26^{th} of January 2019, and the second one is over West ice-shelf (-66.5° latitude, 83° longitude) in East Antarctica on the 8^{th} of February 2019. We preprocessed and downloaded HV backscatter images using the Google Earth Engine (GEE) code editor. Preprocessing steps include the thermal noise removal, radiometric calibration and terrain correction as implemented in the Sentinel-1 toolbox.

3. Methods

The methodology is depicted in Figure 1 and the steps are presented in the following sections.

3.1. Conversion of T_B to the surface frame and preprocessing

The preprocessing applied to SMOS L1C data consists in four steps: i) conversion of the T_{B} from the (XY) antenna frame to the (HV) surface frame, ii) removal of the low-quality and flagged L1C data, iii) incidence angle binning and selection, and iv) solar time calculation.

The first step provides linearly polarized T_{B} defined in the surface frame with its vertical and horizontal components. These are used by most geophysical applications over the ice sheets, such as the melt detection and ice sheet temperature estimation algorithms based on the horizontal and vertical polarization, respectively (Leduc-Leballeur et al., 2020; Macelloni et al., 2019). Hence, the sequences of $T_{\mathrm{B}}^{\mathrm{XX}}$, $T_{\mathrm{B}}^{\mathrm{YY}}$, $Re(T_{\mathrm{B}}^{\mathrm{XY}})$ and $Im(T_{\mathrm{B}}^{\mathrm{XY}})$

measurements given in L1C data are first converted to (T_B^H, T_B^V) pairs. The conversion from the HV surface frame to the XY antenna frame is a simple rotation that requires as input the geometrical and Faraday angles, and the inverse operation needed here converts a sequence of measurements [T_B^{XX}, T_B^{YY}, $Re(T_B^{XY})$, $Im(T_B^{XY})$] to the fully-polarized [T_B^H, T_B^V, 3rd and 4th Stokes components]. We first construct the vector [T_B^{XX}, T_B^{YY}, $Re(T_B^{XY})$, $Im(T_B^{XY})$] for each snapshot, with one exact value and three values obtained through the interpolation of a sequence of close measurements with limited incidence angle variations. The T_B^H and T_B^V in surface frame are then obtained through inversion of the rotation matrix.

In the second step, we discarded the data affected by sun aliases, radio frequency interferences (RFI) and the observations located in the aliased area of a snapshot, as the image reconstruction algorithm is particularly sensitive to noise. For this, we discarded data with the L1C flags (ESA, 2021): *sun point*, *sun glint area*, *alias-free field of view*, *border field of view*, *RFI*, *RFI tails* and *RFI amplitude*. As we noticed additional noise in Greenland that may be due to an incorrect RFI filtering, we also discarded all the observations with a non-physical TB higher than 280 K.

In the third step, we selected different ranges of incidence angle to compute three SMOS enhanced-resolution datasets. The motivation is the large dependence of SMOS L1C spatial resolution on the incidence angle (Figure 2a). The ellipse approximating the -3 dB footprint is larger and more eccentric at higher incidences. The semi-major axis is <20 km for an incidence angle <20° while it is ∼40 km at 52.5° and reaches 90 km near 70°. A careful selection of the L1C data is therefore necessary to obtain an optimum spatial resolution. The first two enhanced-resolution datasets use the observations in a short range of incidences (5°) centered at 52.5° (Single-incidence Enhanced Resolution, SiER$_{52.5}$) near the Brewster angle, and 40° (SiER$_{40}$, at SMAP looking angle), respectively. These incidence bins exist in the L3TB product leading to an easy evaluation of the gain in spatial resolution. The third dataset uses all the observations with an incidence angle lower than 40° (Multi-incidence Enhanced Resolution, MiER). It is designed to exploit the near-nadir observations owing the best native spatial resolution. The low-incidence measurements (< 40°) correspond to the dark blue dots and the red contour in Figure 2.

Figure 2c shows the variations of the radiometric accuracy in H pol (RA$_H$) within a SMOS snapshot (∼1500

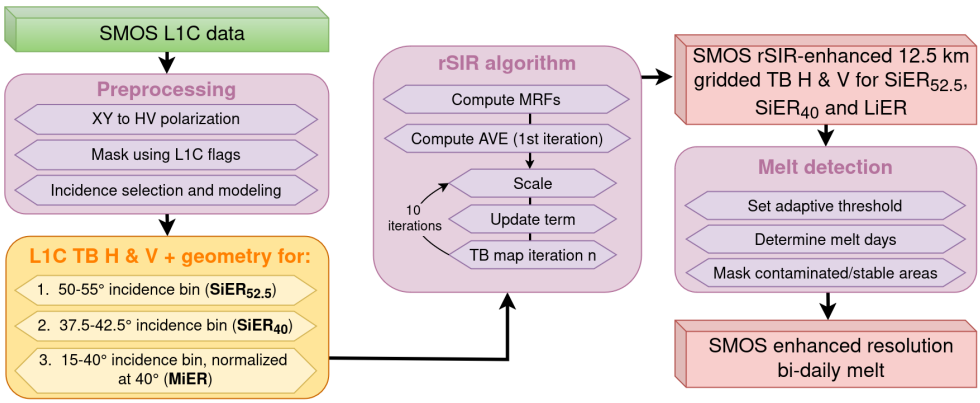

Figure 1: Flowchart of the SMOS resolution-enhancement and melt detection algorithms. The output datasets are highlighted in red boxes.

$\times$ 1500 km^2). RA_H is around 2 K at boresight and is degraded up to 8-9 K along the margins of the snapshot, especially in the cross-track direction. The RA_H is low in the entire area covered once the flagged observations have been discarded, that is in medium blue in Figure 2b, and also after the 40° incidence angle selection (red contour in Figure 2b). The selected observations therefore have a low noise to facilitate the image reconstruction process.

Finally, we separated the morning (before 12 A.M.) and afternoon measurements according to their local solar time which is calculated as $t_{\text{solar}} = t_{\text{UTC}} + \text{longitude}/15$. Morning and afternoon measurements correspond broadly to the ascending and descending passes, respectively.

3.2. Modeling the incidence angle variations

To accommodate the large range of incidence angles in the MiER product, we devised a normalization procedure of the T_{B} to a common equivalent angle, chosen at 40° by convention and for comparability with SMAP. For this, we first modeled the angular variations through a semi-physical approach and then applied this model to scale the T_{B} at 40° incidence. The Multi-Fresnel Thermal Emission (MFTE) model described in detail in Appendix A computes the upwelling radiation emanating from a stack of snow layers with uniform temperature and alternating density values. Given the permittivities ϵ_1 and ϵ_2 of the alternating layers computed from the density values, the model calculates the reflection coefficients in H and V polarizations (R_H, R_V). The modeled brightness temperatures $T^{\text{H}}_{\text{B,model}}$ and $T^{\text{V}}_{\text{B,model}}$ are then calculated as:

$$T^{\text{H}}_{\text{B,model}} = T(1 - R_H) \tag{1}$$

$$T^{\text{V}}_{\text{B,model}} = T(1 - R_V) \tag{2}$$

After a first evaluation, we found that this simple physical model does not perfectly reproduce SMOS incidence diagrams. As an example, Figure 3 presents the morning and afternoon T^{H}_{B} and T^{V}_{B} acquired around Dome

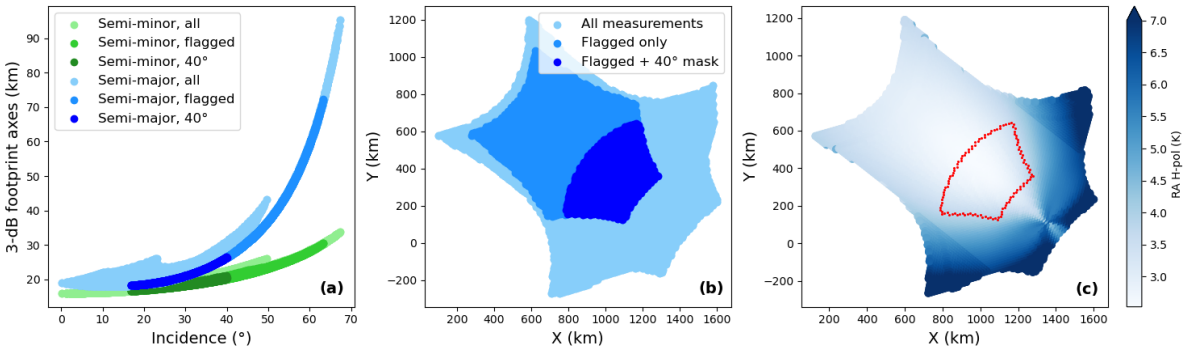

Figure 2: Overview of the L1C flags, radiometric accuracy (RA_H) and spatial resolution variations for one SMOS snapshot on the 19$^{\text{th}}$ of January, 2019. **(a)** Scatterplot of the semi-minor and semi-major axes of the -3 dB antenna footprint against the incidence angle. The light blue and green curves represent all the observations. The medium blue and green curves show the remaining observations once the flagged L1C data have been discarded. The dark blue and green curves show the observations with an incidence angle <40°. **(b)** Location of the non-flagged (remaining) data and the observations with incidence angle <40° within the snapshot, and **(c)** Spatial distribution of RA_H within the snapshot with the contour of the <40° measurements in red.

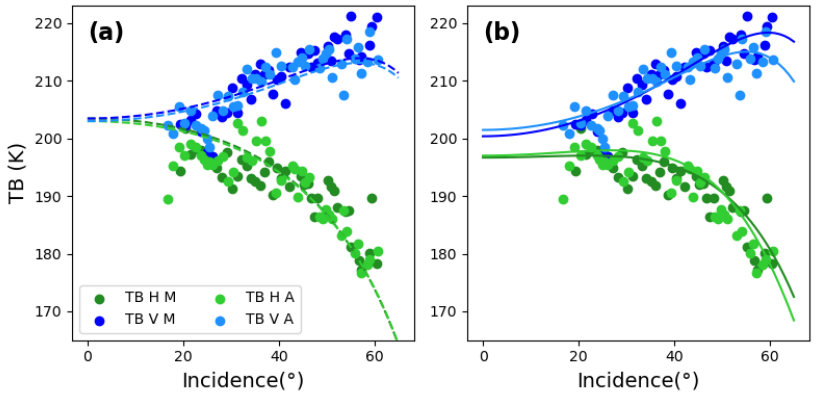

Figure 3: Observed and modeled brightness temperatures as a function of the incidence angle over the DGG n°7144462 close to Dome C on the 19th of January, 2019 for the morning (M) and afternoon (A) passes. In **(a)** the physical multilayer model was fitted to H and V polarized T_{B}. **(b)** is the same for the semi-physical model that includes a linear correction term at H polarization.

C in Antarctica for a single day, as a function of the incidence angle. The dashed lines in Figure 3 were obtained using the MFTE model after fitting both density values. For physical reasons, the modeled T_{B} are constrained in such a way that $T^{\mathrm{H}}_{\mathrm{B,model}}(0^{\circ}) = T^{\mathrm{V}}_{\mathrm{B,model}}(0^{\circ})$. On the contrary, SMOS features significantly lower $T^{\mathrm{H}}_{\mathrm{B}}$ values at low incidence and a steeper variation in $T^{\mathrm{V}}_{\mathrm{B}}$ than the physical model does. To add flexibility in the model, we added an empirical linear term to Equation (1), giving:

$$T^{\mathrm{H}}_{\mathrm{B,model}} = T(1 - R_H)\left(\beta + \alpha(1 - \cos\theta)\right) \tag{3}$$

where the coefficients α and β are unknown. In this case, five unknown parameters need to be estimated: ϵ_1 and ϵ_2 (used to determine R_H and R_V), T, α and β. Note that the physical model is obtained for $\alpha = 0$ and $\beta = 1$. The solid curves in Figure 3 represent the incidence diagrams in Dome C that were computed using the semi-physical model. The constraint at 0° incidence angle is relaxed which allows the model to represent the incidence diagram without bias. We assessed the robustness of this semi-physical model by visual inspections in numerous cases, including over ice shelves in both winter and summer. Because our purpose is to normalize SMOS L1C T_{B} without introducing a bias, which was the case using the physical model only, we adopted the semi-physical approach to compute the MiER product.

Finally, the normalization of SMOS brightness temperatures for the MiER product was performed as follows:

$$T^{p}_{B}(40^{\circ}) = T^{p}_{B}\frac{T^{p}_{B,model}(40^{\circ})}{T^{p}_{B,model}} \tag{4}$$

where p is the polarization. For convenience, the reference angle is set to 40°, to facilitate the comparison with SMAP which has a fixed incidence angle of 40°.

3.3. rSIR algorithm

To retrieve SMOS enhanced resolution T_{B}, we applied the radiometer version of the Scatterometer Image Reconstruction (rSIR) algorithm following Long & Daum (1998) with a few adaptations. This algorithm has been

widely used within the framework of the National Aeronautics and Space Administration (NASA) Making Earth System Data Records for Use in Research Environments (MEaSUREs) program to compute enhanced resolution T_{B} products from SSM/I, SSMIS, AMSR and SMAP on equal-area grids (Long & Brodzik, 2016; Long et al., 2019).

First, the algorithm requires an approximation of the spatial Measurement Response Function (MRF) which represents the smeared antenna gain pattern projected on Earth's surface for every single measurement. Following previous literature (Long & Brodzik, 2016; Brodzik & Long, 2018) and assuming the response is a two-dimensional Gaussian where a half-power point corresponds to the -3 dB footprint contour, the discrete MRF (in dB) of an observation T_i is computed in each pixel p(x, y) as:

$$\mathrm{MRF}_i\,(x,y) = \ln\left(\frac{1}{2}\right)\exp\left(\left(\frac{2\,D_x}{a}\right)^2 + \left(\frac{2\,D_y}{b}\right)^2\right) \tag{5}$$

where a is the semi-major axis and b the semi-minor axis of an ellipse approximating the 3-dB antenna footprint. D_x and D_y are the relative distances from the footprint center to each pixel taken along and across the orientation of the ellipse, respectively. This model was found to be adequate for reconstructing conventional radiometer images (Long, 2015). We investigated this approximation and found it was also valid for SMOS. In the L1 image reconstuction process, a Blackman apodization window is applied to MIRAS synthetic antenna gain to smear the side lobes at the expense of a slightly degraded resolution. This Blackman window can be fitted with good accuracy using a relatively simple centro-symmetric function, as demonstrated for soil moisture inversion in the SMOS L2SM retrieval algorithm (ESA, 2019). If the Gaussian approximation from Long (2015) was used instead, it would have been almost equivalent to the L2SM Blackman within the -3 dB footprint. We therefore assume that Equation (5) correctly represents the MRF of SMOS L1C data.

For each polarization p, we consider a measurement T_i^p as the sum of the brightness temperature T_B^p sampled on the Earth's surface weighted by the MRF:

$$T_i^p = \iint \mathrm{MRF}_i\,(x,y)\,T_B^p\,(x,y)\,dx\,dy \tag{6}$$

The image reconstruction approach in rSIR algorithm aims to estimate the discrete $T_B^p(x,y)$ image from a set of radiometer measurements T_i^p using the modeled MRF_i. Let a_j be the estimated $T_B^p\,(x_j,y_j)$ of the row-scanned j-th pixel. The initialization of the algorithm is performed as a weighted average called AVE:

$$\mathrm{AVE} = a_j^0 = \frac{\sum_i \mathrm{MRF}_{ij}\,T_i}{\sum_i \mathrm{MRF}_{ij}} \tag{7}$$

Then, for every iteration k the algorithm determines the estimated brightness temperature a_j^{k+1} as:

$$f_i^k = \frac{\sum_n \mathrm{MRF}_{in}\,a_n^k}{\sum_n \mathrm{MRF}_{in}} \tag{8}$$

$$d_i^k = \sqrt{T_i / f_i^k} \tag{9}$$

$$u_{ij}^k = \begin{cases} \left[\frac{1}{2 f_i^k} \left(1 - \frac{1}{d_i^k} \right) + \frac{1}{a_j^k d_i^k} \right]^{-1} & , d_i^k \geq 1 \\ \left[\frac{1}{2} f_i^k \left(1 - d_i^k \right) + a_j^k d_i^k \right] & , d_i^k < 1 \end{cases} \tag{10}$$

$$a_j^{k+1} = \frac{\sum_i \mathrm{MRF}_{ij} u_{ij}^k}{\sum_i \mathrm{MRF}_{ij}} \tag{11}$$

where f_i^k is called the forward projection, d_i^k is the scale factor and u_{ij}^k is the update term (Long & Daum, 1998).

This process is iterated K times. Long & Daum (1998); Long & Brodzik (2016) noticed that both the reconstruction accuracy and the noise level increase while iterating. K was set to 10 iterations in our algorithm as this value permits a good tradeoff between noise and reconstruction accuracy. It is lower than the 20 iterations used for SSM/I in Long & Brodzik (2016) to account for the higher noise in the interferometric MIRAS measurements compared to conventional radiometers, ∼2 K vs <1 K for SMAP (Piepmeier et al., 2017) and AMSR C, X, K and Ka bands (Imaoka et al., 2010). After 10 iterations, the reconstruction accuracy converges towards an asymptotic value with few changes compared to 15 or 20 iterations (also evaluated), while the noise level increases rapidly.

The enhanced-resolution T_B maps were computed the same way for both H and V polarizations and morning and afternoon passes over the entire 14-year SMOS dataset, for the $\mathrm{SiER}_{52.5}$, SiER_{40} and MiER products.

3.4. Evaluation of the effective spatial resolution

We defined a common methodology to evaluate and compare the effective spatial resolution of six datasets: the three new SMOS rSIR-enhanced datasets based on the L1C data ($\mathrm{SiER}_{52.5}$, SiER_{40} and MiER), the SMAP rSIR-enhanced T_B and the SMOS L3TB at both 52.5° and 40° incidence angles. The effective spatial resolution is defined here as the Full Width at Half Maximum (FWHM) of the Pixel Spatial Response Function (PSRF), which is modeled as a two-dimensional Gaussian. The FWHM is related to the standard deviation σ of the Gaussian through:

$$\mathrm{FWHM} \; = \; 2\sqrt{2\ln(2)}\,\sigma \; \approx \; 2.355\sigma \tag{12}$$

To determine the FWHM for each dataset, we adopted a similar procedure as in Long et al. (2023). We first identified a suitable region with an abrupt and large spatial transition, such as between the ice-sheet and the ocean. This transition is modeled as a two-dimensional step function. The convolution of 2D Gaussian kernels of varying FWHM with this step function is compared to the observed T_B to determine the smoothness of brightness temperature changes. We minimize the Root Mean Square Error (RMSE) between the convoluted and observed data to find the optimal FWHM corresponding to the estimated spatial resolution. The RMSE was computed along a transect perpendicular to the coastline instead of the whole image.

The step function is defined here using Sentinel-1 HV images to delineate the ice and ocean surfaces which correspond to the maximum and minimum expected brightness temperatures, respectively (see Figure 4, left

column). Two case studies are investigated, over the western Antarctic Peninsula on January 26th, 2019 and over West ice shelf in East Antarctica on February 8th, 2019.

3.5. Liquid water detection

The presence of liquid water in the snowpack is detected using the adaptive-threshold algorithm published in Leduc-Leballeur et al. (2020) with very few changes. This algorithm for SMOS stems from an earlier algorithm designed for 19 GHz observations acquired by SMMR and SSM/I (Torinesi et al., 2003), and further improved by Picard & Fily (2006) with successful applications to SSMIS, AMSR-E and AMSR2 (e.g. (Saunderson et al., 2022)).

In brief, the sharp increase in T_{B} time series caused by the liquid water appearance is detected using a threshold value computed as:

$$T = M + 3 \times \sigma \tag{13}$$

where M is the average and σ is the standard deviation of $T_{\mathrm{B}}^{\mathrm{H}}$ calculated in dry snow days only, from the 1^{st} of April to the 31^{st} of March. The problem is circular as the knowledge of melt days is required to exclude them from the computation of M and σ, which are further used to detect melt. This is resolved by first detecting melt using the all-day annual average for M and a fixed value of 15 K for 3σ. The first-guess melt time series is then used to update M and σ. Three iterations are performed to obtain the definitive threshold, used to compute the final melt time-series.

Noting that false alarms occur in the interior of the Antarctic ice-sheet where melt is obviously absent, we identified and masked these areas by excluding the pixels where the standard deviation of $T_{\mathrm{B}}^{\mathrm{V}}$ exceeds 2.8 K, following Leduc-Leballeur et al. (2020). As this threshold was optimized for Antarctica, it was reevaluated and set to 5 K on Greenland where we noticed a higher variability in SMOS T_{B} time series.

In Antarctica, coastal pixels also show frequent false alarms due to ocean contamination of the radiometric signal. The higher T_{B} on sea-ice than on open ocean indeed leads to a large and erroneous detection of winter melt days along the coastlines. Winter melt may occur on multiple Antarctic ice shelves due to foehn wind (Kuipers Munneke et al., 2018) or atmospheric rivers (Wille et al., 2019), but with much lower recurrence. Hence, we computed a contamination mask over Antarctica that filters out the pixels where the winter melt occurrence overpasses 5 % in the entire 14-year melt time series. In Greenland, where winter melt is more frequent, the contamination mask is not needed due to the much lower number of marine-terminating glaciers.

4. Results

We produced three twice daily SMOS rSIR-enhanced datasets based on the L1C product for the period 2010-2024: the SiER$_{52.5}$, SiER$_{40}$ and MiER. The coverage of these datasets and the radiometric comparison against the SMOS L3TB product are first presented. Then, we evaluate the spatial resolution of each product in two case studies. Finally, we apply the melt detection algorithm and analyze the benefit of the resolution enhancement for this application.

Table 1: Average percentage of the AIS pixels revisited in one or two days for the MiER, $SiER_{40}$ and $SiER_{52.5}$ products. The coverage was evaluated for morning and afternoon tracks separately, and also for the daily average of all the tracks.

		rSIR morning	rSIR afternoon	rSIR daily
1-day coverage (%)	**MiER**	90.1	91.1	98.0
	$SiER_{40}$	93.7	94.5	99.2
	$SiER_{52.5}$	92.2	93.3	98.6
2-day coverage (%)	**MiER**	99.4	99.7	99.9
	$SiER_{40}$	99.6	99.7	100.0
	$SiER_{52.5}$	99.3	99.6	99.7

4.1. SMOS rSIR-enhanced products

Table 1 presents the percentage of Antarctic pixels revisited every day and at least every two days for the $SiER_{52.5}$, $SiER_{40}$ and MiER datasets. The revisit was computed for the daily average of all tracks and for morning and afternoon tracks separately throughout one year (2019). For the three evaluated datasets, the morning and afternoon tracks cover each more than 90 % of the AIS within one day and >99 % of the AIS within two days. Hence, the SMOS rSIR-enhanced datasets are suitable to detect daily or sub-daily T_{B} variations associated to a melt signal.

The radiometric quality of the SMOS rSIR-enhanced datasets was evaluated by comparing to the 40° and 52.5° incidence bins of the L3TB product. Table 2 presents the mean difference (MD) and the Root Mean Square Deviation (RMSD) computed over Antarctica and Greenland in 2019 for all the pairs of datasets compared. We expect a low MD as an indicator of the consistency of each dataset, and a RMSD very low on the stable areas of the Antarctic plateau but much higher on the periphery of the ice sheet where most of the differences due to the resolution enhancement are concentrated. Compared to the L3TB product at 40°, the results show a higher MD for the MiER (+1.16 K to +1.6 K for H, -0.64 K to -0.97 K for V) than for the $SiER_{40}$ (<0.75 K). The $SiER_{52.5}$ dataset also shows a low MD compared to the L3TB product at 52.5° (<0.33 K). For all the datasets, we obtain a consistent RMSD between 2 K and 4 K with most of the differences concentrated near the coastlines. Only the MiER shows a systematic high MD in the dry and homogeneous Antarctic plateau. The MD is positive for the horizontal polarization and negative for the vertical polarization, which may indicate a bias caused by issues in the incidence diagram modeling. None of the incidence diagrams inspected show an anomalous pattern, but numerical issues in the least square fit could lead to finding a wrong local minimum. This problem requires further investigation to fully exploit the valuable geophysical information contained in SMOS incidence diagrams.

Table 2: Mean difference (MD) and Root Mean Square Deviation (RMSD) over 1 year (2019) between the SMOS rSIR-enhanced datasets and the SMOS L3TB at both 40° (MiER, $SiER_{40}$) and 52.5° ($SiER_{52.5}$) incidence angle over Antarctica and Greenland. All units are in Kelvin (K).

		MD H	MD V	RMSD H	RMSD V
Antarctica	**MiER**	1.60	-0.97	3.15	2.68
	$SiER_{40}$	0.75	0.41	2.91	2.40
	$SiER_{52.5}$	-0.07	0.08	2.23	1.71
Greenland	**MiER**	1.16	-0.64	3.86	3.60
	$SiER_{40}$	0.41	0.31	3.90	3.42
	$SiER_{52.5}$	-0.02	0.33	3.10	2.64

4.2. *Evaluation of the effective spatial resolution*

The effective spatial resolution is evaluated in two case studies presented in Figure 4: the West ice shelf (East Antarctica, top row) and the Anvers Island (Antarctic Peninsula, bottom row). The first column shows the 2D land/ocean step function derived from Sentinel-1 and the other columns show four $T_{\mathrm{B}}^{\mathrm{V}}$ maps at 40° incidence: the SMAP rSIR-enhanced from Long et al. (2019), the SMOS rSIR-enhanced MiER (15-40°) and SiER_{40} (40°), and the SMOS L3TB. We normalized the $T_{\mathrm{B}}^{\mathrm{V}}$ maps between 0 and 1 to compare measurements performed by different sensors. Qualitatively, the spatial resolutions of the SMAP enhanced and the two SMOS enhanced maps look similar although the grid is four times finer in SMAP (3.125 km against 12.5 km). The SMOS L3TB at 40° shows a larger land-ocean transition indicating a lower spatial resolution in both case studies. For instance, the local T_{B} maximums at the locations of Anvers and Brabant islands as well as the channel separating these islands from the continent are well identified in all the SMAP rSIR and SMOS rSIR products. These features are smoothed in the SMOS L3TB where a continuous gradient from ocean to land is rather observed.

Quantitatively, the spatial resolution was estimated along two transects (red lines in Figure 4). Figure 5

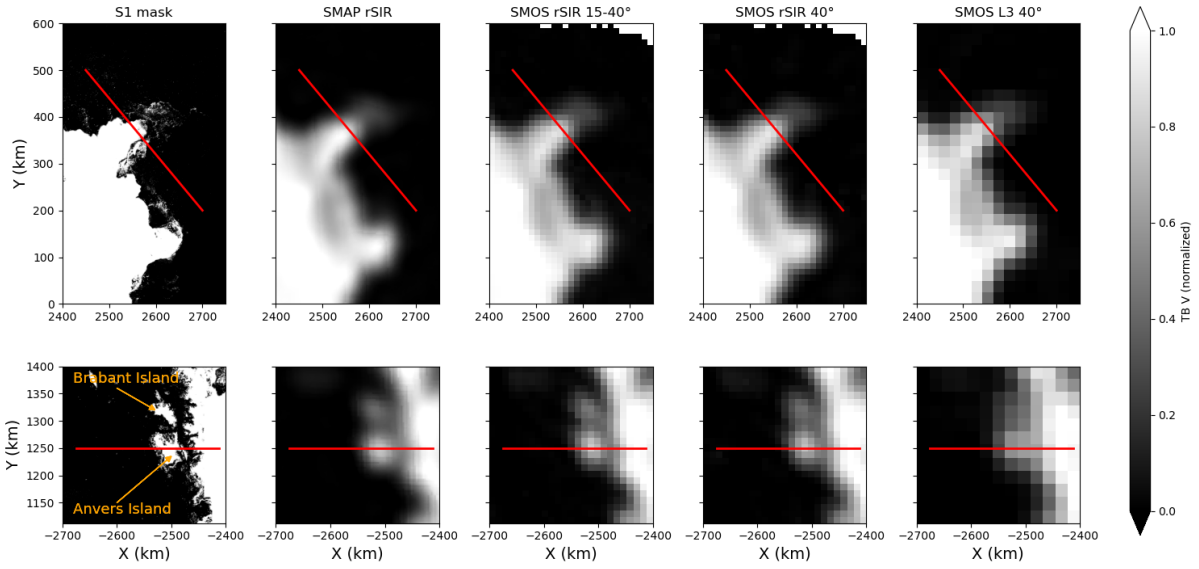

Figure 4: Normalized $T_{\mathrm{B}}^{\mathrm{V}}$ for the ideal S1 mask, SMAP rSIR-enhanced evening tracks, SMOS rSIR-enhanced multi-incidence (15-40°) and single-incidence (40°) afternoon passes and SMOS daily L3TB products over the West ice-shelf on February 7-9th, 2019 (top row) and over Anvers Island on January 25-27th, 2019 (bottom row). The red lines show the transects used to compute the effective spatial resolution of each product in Figure 5.

Table 3: Estimated spatial resolution along two transects over the West ice-shelf and Anvers island, using six datasets: the SMOS L3TB at 52.5° and 40°, the SMOS rSIR-enhanced SiER**40**, SiER**52.5** and MiER, and the SMAP rSIR-enhanced at 40°. For each dataset both the H-pol and V-pol spatial resolution were computed.

Dataset	**Spatial resolution (km)**			
	Anvers H	**Anvers V**	**West H**	**West V**
SMOS L3TB 52.5°	55	53	60	58
SMOS L3TB 40°	47	45	44	42
SMOS rSIR 52.5°	47	45	48	45
SMOS rSIR 40°	33	32	31	30
SMOS rSIR 15-40°	33	31	33	30
SMAP rSIR	31	30	28	28

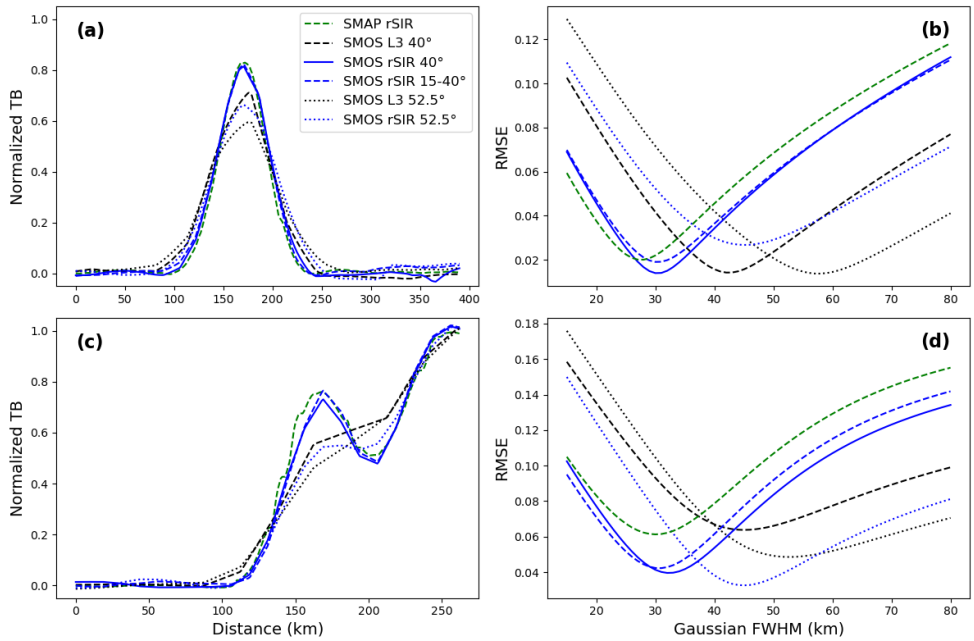

Figure 5: Estimation of the effective spatial resolution along two transects for the West ice shelf (a, b) and Anvers Island (c, d) case studies (see Figure 4 for the locations of these transects). **(a, c)** T_{B} plotted along the transects, **(b, d)** RMSE between the observed and convoluted images plotted against the FWHM of Gaussian kernels used for convolution. The estimated effective spatial resolutions are the FWHM at minimum RMSE for each dataset.

presents the normalized $T_{\mathrm{B}}^{\mathrm{V}}$ along these transects (a, c), and the RMSE computed between the observed and convoluted images as a function of the Gaussian FWHM (b, d). For all the datasets evaluated, the RMSE decreases until reaching a minimum where the observed and convoluted maps match the best and then increases again. The FWHM of the modeled transect at the minimum of RMSE is the estimated effective spatial resolution. It is reported in Table 3 for all the six datasets and for both case studies in H and V polarizations. The results are very close for each location and polarization showing the robustness of the estimation. The MiER, SiER$_{40}$ and SMAP rSIR-enhanced T_{B} maps have the finer spatial resolution, around 30 km, while the SMOS L3TB at 40° has a spatial resolution of 42-47 km. Note that the footprints of native observations used to reconstruct the SiER$_{40}$ and SMAP rSIR-enhanced datasets are similar (39 $\times$ 47 km for SMAP, $\sim$41 $\times$ 53 km for SMOS at 40° incidence). This is a good reason to believe that the rSIR algorithm was correctly implemented and adapted in this study. At 52.5° incidence, the SiER$_{52.5}$ product has a spatial resolution of 45-48 km and the SMOS L3TB is in the range of 53-60 km. The SiER$_{40}$ product therefore improves the spatial resolution by 40-50 % compared to the L3TB at 52.5°, half of the enhancement being due to the reconstruction algorithm (rSIR) while the other half is due to the lower incidence angle used here. Based on these results, we further used the SiER$_{40}$ product to assess the impact of resolution enhancement on melt detection.

4.3. Impact of the resolution enhancement on melt detection

4.3.1. Ice-sheet wide comparison of melt detection

We calculated the 14 year-long (April 2010 - March 2024) time series of melt in Greenland and Antarctica using the original SMOS L3TB product at 52.5° and the new rSIR-enhanced SiER$_{40}$ product, using the melt detection

algorithm presented in Leduc-Leballeur et al. (2020) and Section 3.5. Note that twice-daily melt was computed from the rSIR-enhanced dataset while the L3TB melt only includes a daily estimation which combines morning and afternoon tracks.

The average annual number of melt days according to the enhanced product is shown over Antarctica in Figure 6. It is particularly high over the Antarctic Peninsula, with up to 100 days per year on average on the Wilkins ice shelf. Other regions with a large and recurrent melt signal are located all around Antarctica, on the Riiser-Larsen, Fimbul, Roi Beaudoin, Amery, West, Shackleton and Abbott ice shelves. Additionally, more localized melt patterns with a lower extent and/or less than 30 melt days per year can be distinguished, for example in Wilkes Land.

The difference between the average annual number of melt days computed using the $SiER_{40}$ product and the SMOS L3TB at 52.5° is shown in Figure 7. The pink color represents regions where the enhanced dataset detects more melt than the L3TB, and conversely the green color represents regions with less melt than in the L3TB. The dominant pink color on the map clearly demonstrates that the resolution enhancement makes it possible to capture a longer and wider melt signal over all the Antarctic ice shelves. We found above 30 additional melt days in several regions. This is especially the case near the grounding line (dashed lines in Figure 6 and Figure 7) where the transition from dry to wet snow is sharper in the enhanced resolution dataset. Moreover, the green areas are often very localized on the grounded ice sheet just upstream the grounding line, *e.g.*, for the George VI, Larsen C, Roi Beaudoin and Shackleton ice shelves, suggesting false-positives (*i.e.*, over-estimation) in the L3TB

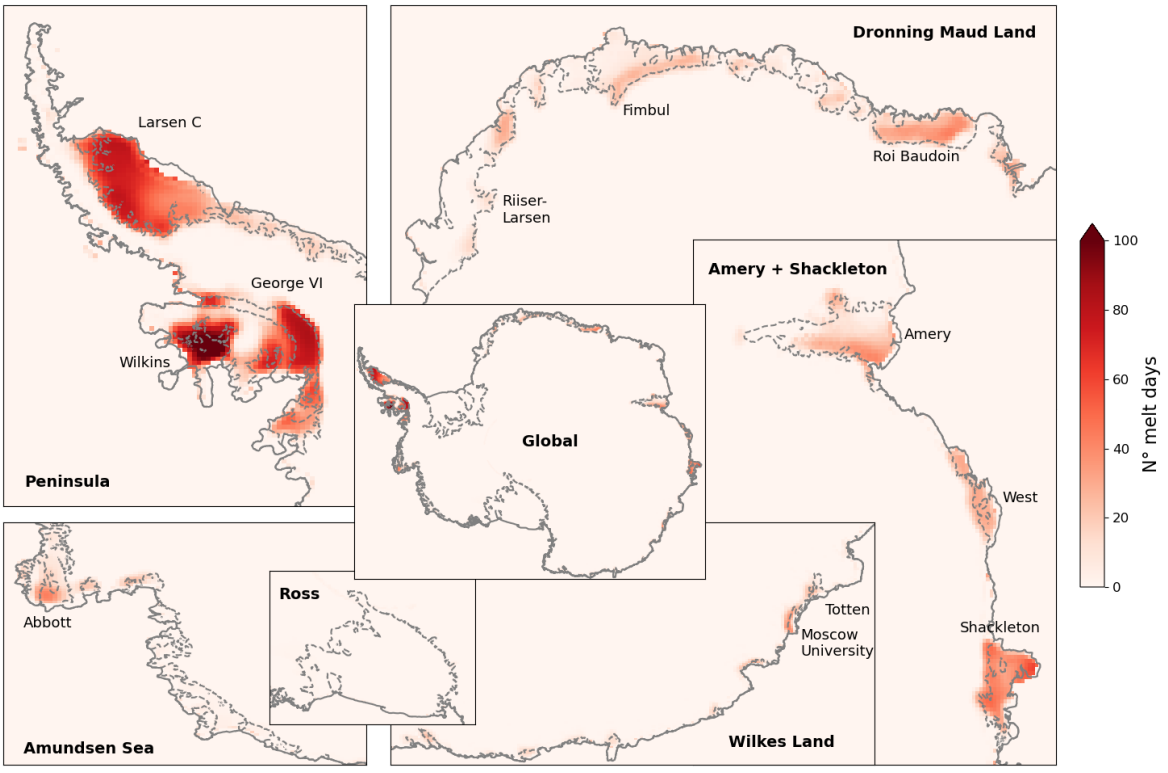

Figure 6: 2010-2024 annual average number of melt days detected using SMOS rSIR-enhanced resolution dataset over Antarctica.

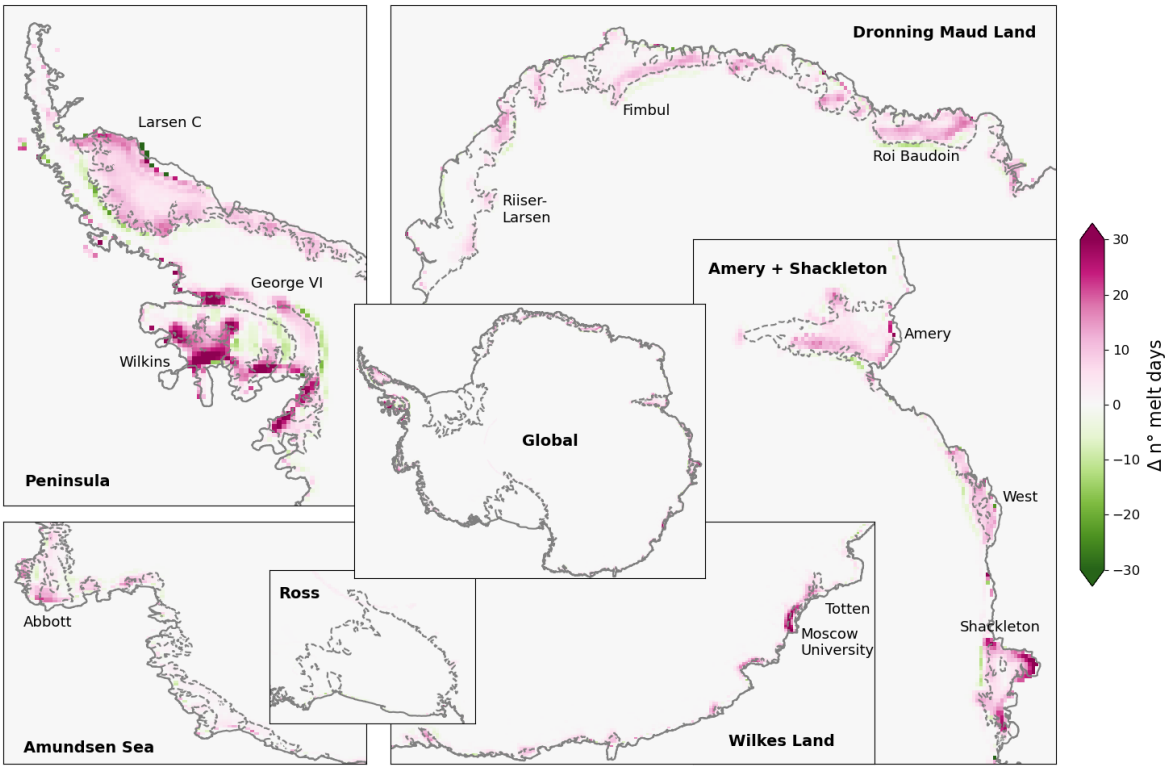

Figure 7: Difference between the 2010-2024 annual average number of melt days detected using SMOS rSIR-enhanced and SMOS L3TB datasets. A higher number of melt days in the enhanced resolution product is shown in pink.

due to the spreading of the wet snow signal. We also notice that in some regions the L3TB product indicates no melt days at all, while the enhanced resolution dataset captures more than 10 melt days per year on average, such as in Wilkes Land on the Moscow University and Totten ice shelves.

The number of melt days detected by the L3TB and SiER_{40} products over Greenland and their differences are shown in Figure 8 for each melt year from 2010 to 2023. Several remarks can be inferred. First, when compared to the L3TB, the SiER_{40} melt presents similar spatial patterns with intense melt on the contour of the ice-sheet. A large number of melt days is observed in the southeast and southwest Greenland particularly. This is coherent with previous studies reporting the presence of perennial firn aquifers and ice slabs in these regions (Koenig et al., 2014; Miège et al., 2016; Miller et al., 2020, 2022). The interannual variability is well represented with an exceptional melt season in 2012 which was identified and studied in the literature (Nghiem et al., 2012).

Large differences between the L3TB and SiER_{40} melt in Greenland affect most of the melting areas around the ice sheet. As in Antarctica, the SiER_{40} product consistently features a larger number of melt days (about +30) compared to the L3TB product in many locations and especially along the southeastern coast. On the contrary, the number of melt days is larger in the L3TB on thin bands located in the upper part of the melting regions. This localized larger melt signal in the lower resolution L3TB could be due to both the conservative 5 K threshold on T_{B}^{V} used to define the dry snow mask on Greenland for the SiER_{40} product, and to the mixing of dry and wet snow regions in the L3TB, as noted in Antarctica around the grounding line. The effect of the conservative 5 K threshold adopted is noticeable elsewhere, for example in 2023 where the baseline product based on the

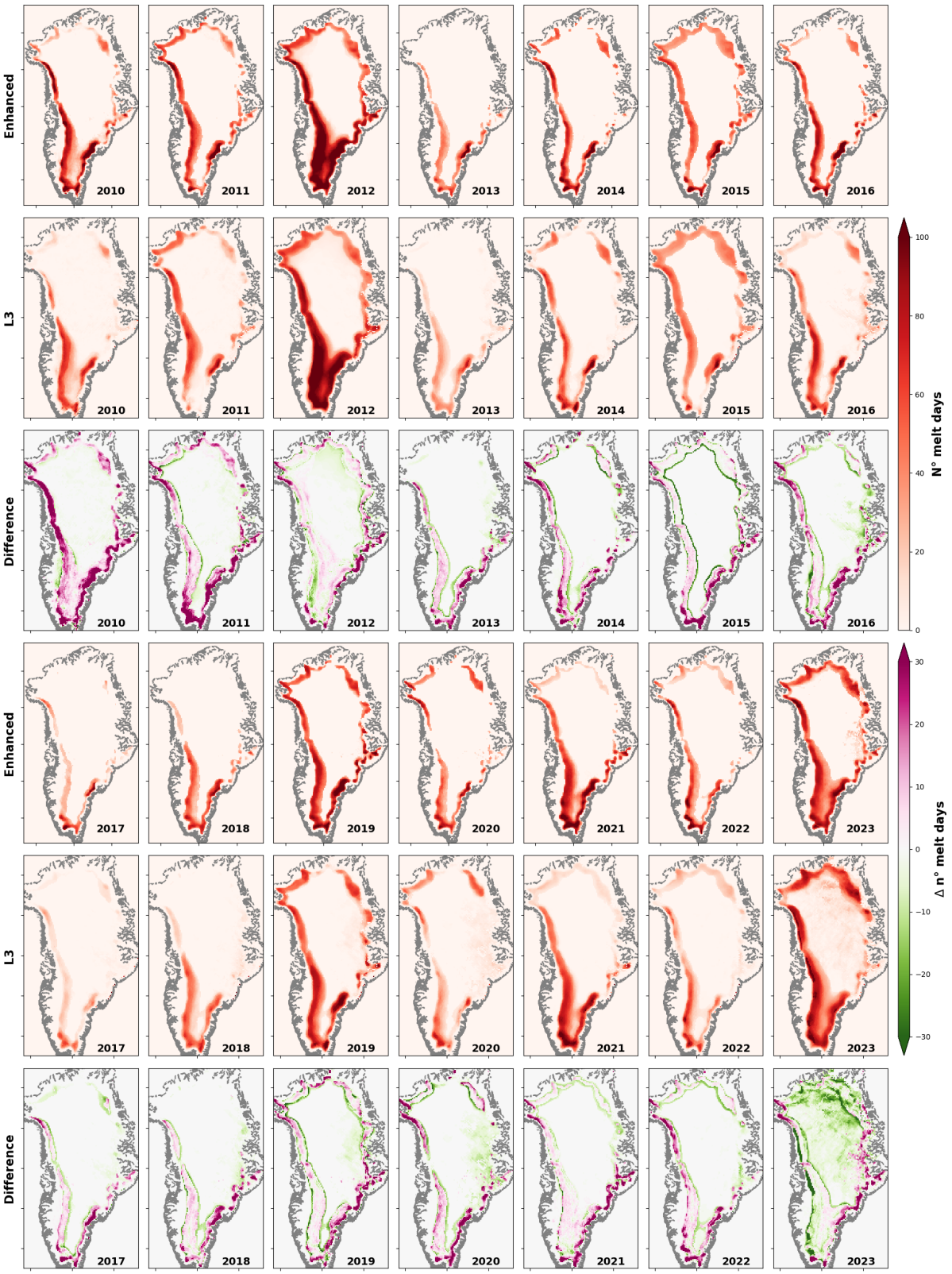

Figure 8: Annual number of melt days detected over Greenland using the SMOS MiER, L3TB and the difference between both products. Fourteen melt years from 2010-2011 to 2023-2024 are presented in the panels.

L3TB features many false alarms in the East and Northeast Greenland while these regions are filtered out in the enhanced resolution product.

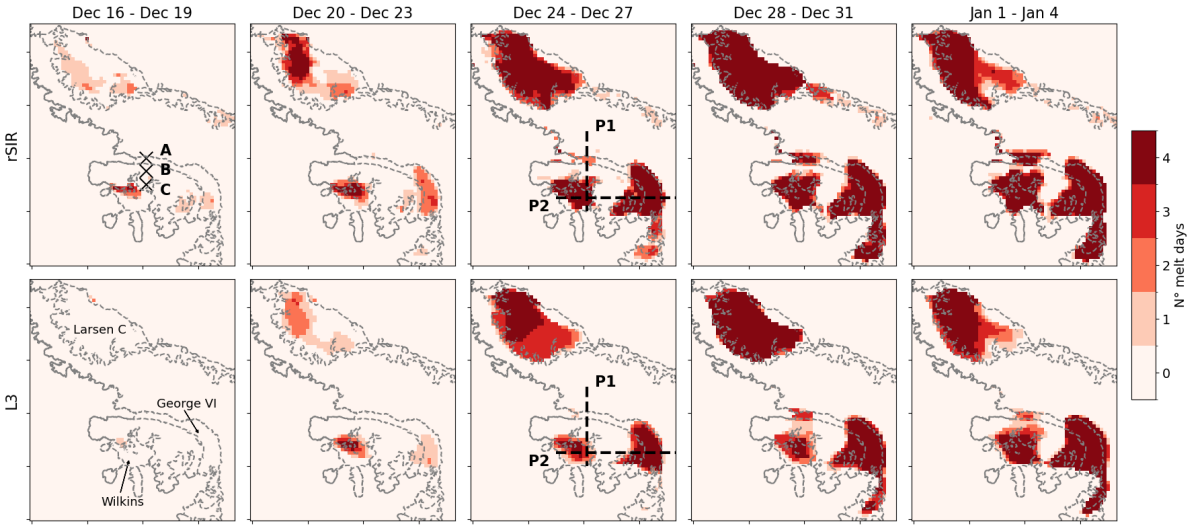

Figure 9: Illustration of the melt onset in the Antarctic Peninsula in 2018-2019. Each map shows the number of melt days over a 4 day period for rSIR (top row) and L3TB (bottom row). Pixels A, B and C correspond to the time series in Figure 11 and P1 and P2 represent the transects shown in Figure 10.

4.3.2. Investigation of a melt event in the Antarctic Peninsula

To further investigate the reason of the larger number of melt days detected in the SiER_{40} product, we focus on a specific melt event. Figure 9 shows the number of melt days on the Antarctic Peninsula in five consecutive 4 day periods from December 16, 2018 to January 4, 2019. Going into the summer, melt propagates rapidly to the entire Wilkins, George VI and Larsen C ice shelves. Melt is detected earlier and with a wider extent in the SiER_{40} product (top row) compared to the L3TB product (bottom row), especially in the northern George VI ice shelf.

Figure 10 presents the difference between the average T_{B}^{H} on December 24-27$^{\text{th}}$, 2018 and the average winter T_{B}^{H} ($\Delta T_{\text{B}}^{\text{H}}$) along the transects P1 and P2. P1 crosses the Wilkins and northern George VI ice shelves, while P2 crosses the Wilkins, Bach and Southern George VI ice shelves (see Figure 9). We also show the melt detection threshold along P1 and P2 for the L3TB and rSIR products to identify areas where $\Delta T_{\text{B}}^{\text{H}}$ is larger, corresponding to melting regions detected by the adaptive threshold algorithm. A large peak in $\Delta T_{\text{B}}^{\text{H}}$ is associated to the crossing of each ice shelf. This peak in summer T_{B} is also present but smoothed in the L3TB product. This results in the SiER_{40} product rising above the melt detection threshold more frequently than the L3TB. On the northern George VI ice shelf (P1, right peak), the L3TB product does not reach the melt detection threshold while the SiER_{40} does. This mainly explains the large increase in annual melt days observed in the northern George VI ice shelf when using the new enhanced resolution dataset compared to the L3TB (see Figure 7).

To explain further the differences observed between the number of melt days detected by the two products, Figure 11 presents the time series of T_{B}^{H} at the locations of pixels A, B and C shown in Figure 9. The melt days detected by the L3TB product (green bars) and the SiER_{40} (blue bars) are indicated at the bottom of each plot. Pixel A is located on the northern George VI ice shelf. Here, the peak in T_{B}^{H} is smoothed in the L3TB compared to the SiER_{40}, and as a consequence the latter indicates more melt (63 days) than the former (48 days). Pixel

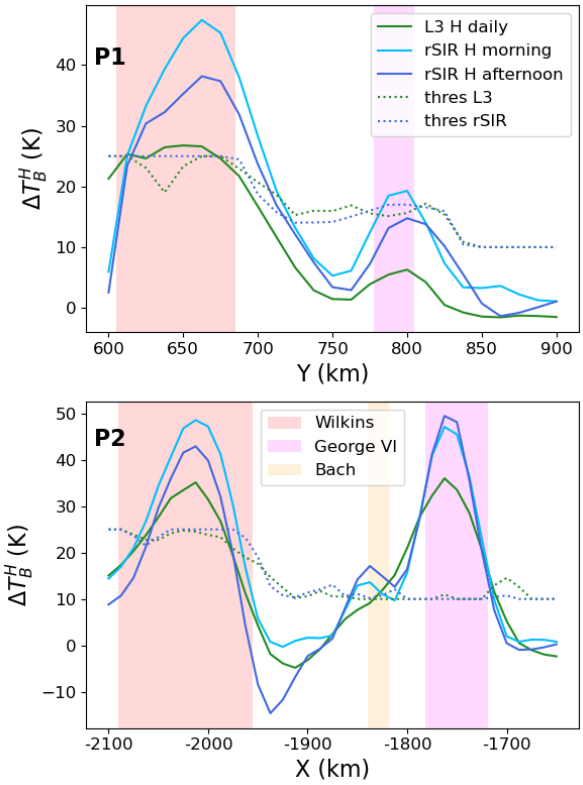

Figure 10: Difference ($\Delta T_{\mathrm{B}}^{\mathrm{H}}$) between the average $T_{\mathrm{B}}^{\mathrm{H}}$ on December 27-30th, 2018 and the average winter $T_{\mathrm{B}}^{\mathrm{H}}$ computed from June 1st to August 31st, 2018, along two transects in Y (P1) and X (P2) crossing the George VI and Wilkins ice shelves. P1 and P2 are identified in Figure 9 which also shows the intensive melt occurring during the 4-day interval on both ice shelves.

B is located on the mountain range separating the George VI and Wilkins ice shelves. Here, melt is less likely due to higher altitude (mountain ranges >1500 m) and results mainly from the contamination of SMOS signal by surrounding wet snow areas. The amplitude of $T_{\mathrm{B}}^{\mathrm{H}}$ variations in the SiER$_{40}$ is lower than in the L3TB, which results in a lower number of melt days (16 instead of 31). Finally, pixel C is located nearby the grounding line of Wilkins ice shelf in a region with intense melt. Both products show a strong seasonal increase in $T_{\mathrm{B}}^{\mathrm{H}}$ and the number of melt days detected is slightly higher in the SiER$_{40}$ (68 days) than in the L3TB (60 days).

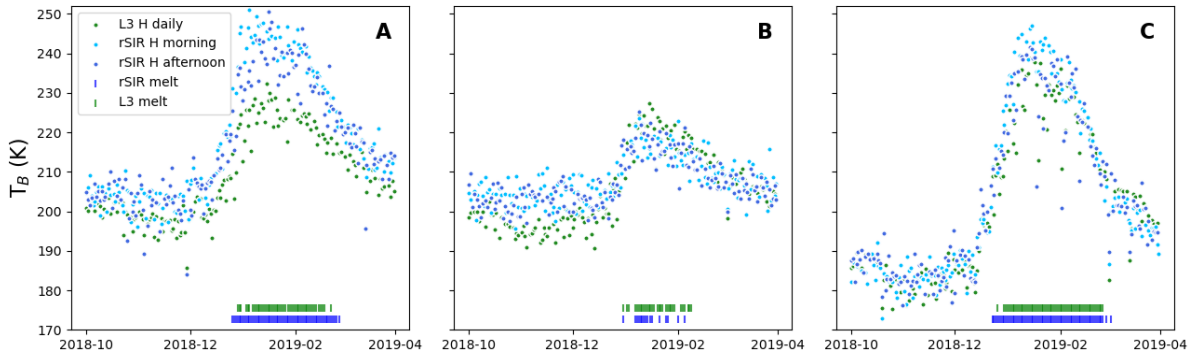

Figure 11: Time series of $T_{\mathrm{B}}^{\mathrm{H}}$ for SMOS L3TB and SiER$_{40}$ products from April 2018 to March 2019 for the pixels marked at locations A, B and C in Figure 6 and Figure 7 on Antarctic ice shelves. The blue (green, respectively) bars at the bottom of each subplot indicate the days where melt is detected using the SiER$_{40}$ (L3TB).

5. Discussion

We have used the SMOS L1C as the unique input of the well-established rSIR algorithm to reconstruct enhanced resolution T_{B} maps for SMOS, in order to assess the possible gain in spatial resolution and the impact on melt detection. This process involved several methodological choices and adaptations of the baseline algorithms that are discussed in this section.

5.1. Tradeoff between noise, coverage and spatial resolution

The application of the rSIR algorithm to SMOS involved several critical choices which were made for a targeted application, the melt detection. We discuss here these choices and their influence on the balance between noise level, spatial resolution and coverage, and how they could be adjusted for other applications.

A first tradeoff between the noise and the coverage is related to the choices of the poor data rejection criteria. The area within a SMOS snapshot with lowest noise is centered along-track at approximately 35-40° incidence angle, while the noisiest parts are located near nadir and close to the border of the track, as shown in Figure 2c. The selection of the best data only tends to reduce the width of SMOS tracks. Melt detection can accommodate a higher noise as it consists in detecting T_{B} variations of several tens of Kelvin, while the best possible coverage is required to follow its daily or sub-daily variations. The SiER_{40} product was therefore computed accepting a high radiometric accuracy threshold of 5 K for a single measurement and it achieves a coverage of 99 % of the Antarctic pixels every day. As a consequence, the average radiometric accuracy is high (<2 K) in the center and lower ($\sim$4 K) near the border of the tracks. Other applications requiring higher accuracy should reject more data and deal with a reduced coverage or temporal revisit.

A second tradeoff is between noise and spatial resolution, and depends on two settings. Firstly, the measurements with lowest radiometric accuracy are located at boresight (32.5° incidence in the along-track direction). Low-incidence observations are likely noisier but also have the highest native spatial resolution (see Figure 2) which led us to select incidence bins at 40° and lower. Low-incidence measurements could be excluded for other applications to ensure a better radiometric accuracy. Secondly, the number of iterations in the image reconstruction process controls the enhancement and the noise of T_{B} maps. The rSIR algorithm was applied in previous studies to conventional radiometers with low noise ($\sim$1 K or lower, (Long & Brodzik, 2016; Long et al., 2019)). In principle, the use of noisier raw data from SMOS logically limits the achievable spatial resolution of the image reconstruction as the iterations must be stopped earlier. For this reason, a threshold of 10 iterations is adopted in this study for SMOS which is lower than the typical 20 iterations threshold of the NSIDC products for SSM/I, SSMIS, AMSR-E and SMAP (Long & Brodzik, 2016; Long et al., 2019). This may explain the slightly reduced effective spatial resolution of the SiER_{40} compared with the SMAP rSIR-enhanced product (difference $\leq$3 km, Table 3). In practice, the selection of observations with a larger radiometric accuracy (e.g. located on the border of the tracks) does not seem to have a strong impact on the reconstruction of SMOS T_{B}, as we obtained an equivalent spatial resolution for the range of accuracy 2.8–5 K. We also found that a reconstruction with 15 iter-

ations (not shown) provided no significant improvement in spatial resolution, but a higher noise. The potential of further resolution enhancement for SMOS using the rSIR algorithm is therefore likely limited.

5.2. Multi-incidence dataset

The use of multi-incidence measurements from $\sim$15° to 40° in the MiER product aimed to select data with the best native spatial resolution, but it requires to normalize the variations of T_{B} depending on the incidence angle using the MFTE model. It turns out that the physical model is unable to reproduce SMOS incidence diagrams, especially close to nadir. A similar issue was observed between SMOS incidence diagrams and the in-situ L-band radiometer RADOMEX installed at Dome C in 2010 (see Figure 14 in Macelloni et al. (2013)). We suspect that the conversion of the measurements from the XY antenna frame to the HV surface frame used in geophysics could be responsible for this non-physical behavior. A direct use of XY brightness temperatures in geophysical applications is less common but could prevent this issue. In our approach, we used a more flexible semi-physical model to fit SMOS incidence diagrams as we are only interested in the normalization of all observations to a fixed incidence angle.

During the evaluation of the spatial resolution, we observed that the MiER and SiER_{40} products have almost the same resolution (see Table 3). As our results suggest that the additional complexity and computing cost of the multi-incidence approach are not worth the result, we finally adopted the SiER_{40} product to detect melt. We have three hypotheses to explain why the inclusion of low-incidence observations does not enhance the resolution. First, the gain in native spatial resolution from 40° to the lowest incidence is relatively small compared to the large improvement between 55° and 40° (Figure 2a). Secondly, SMOS observations near nadir have a small spatial coverage so the reconstructed brightness temperature maps are dominated by data near 40°, especially close to the border of the tracks. Thirdly, the lowest incidence data have a higher radiometric accuracy which could limit the capability of the rSIR algorithm to reconstruct accurate T_{B} images. Overall, for applications requiring the knowledge of complete SMOS incidence diagrams with an enhanced resolution, a practical solution would be to compute enhanced resolution T_{B} maps for each incidence bin in the L3TB product.

5.3. Limitations and improvements of melt detection

The algorithm proposed in Leduc-Leballeur et al. (2020) to detect melt from the L3TB product requires minor modifications to be applicable to the enhanced resolution product. The characteristics of this new product and the necessary technical adjustments may have an impact on the melt detection algorithm in three different ways.

First, we had to modify the mask introduced in Leduc-Leballeur et al. (2020) to filter out regions where snow is always dry. In Antarctica, it concerns all the pixels where the standard deviation on $T_{\mathrm{B}}^{\mathrm{V}}$ is lower than 2.8 K. This approach works well in Antarctica, but in Greenland we had to increased the threshold to 5 K to deal with the larger T_{B} variability. The additional noise in Greenland may be due to an incorrect RFI filtering using L1C flags, as we noticed a bunch of observations with T_{B} as large as 400 K. These outliers were filtered out using

a simple thresholding. All the measurement with a T_B higher than 280 K are considered as non-physical and potentially affected by RFI, which is a fair assumption on the ice sheets. However, some observations with a T_B lower than 280 K could still be affected by RFI and introduce noise in the reconstructed maps.

Secondly, the new SiER$_{40}$ product is noisier than the L3TB at 52.5° (Section 5.1) which is susceptible to disturb the melt detection algorithm. Isolated false alarms may occur due to outliers but this effect is difficult to evaluate, as it is also counterbalanced by the increase of the 3σ melt detection threshold due to higher noise. This higher 3σ threshold can also reduce detection early and late in the season with the enhanced resolution product. However, this effect seems negligible given the otherwise considerable larger number of melt days observed throughout Antarctica and Greenland in the SiER$_{40}$ compared to the L3TB (see Figure 6 and Figure 7), corresponding to a clear snow wetting with large T_B variations as shown in Figure 10 and Figure 11.

Lastly, we used data with an incidence angle of 37.5–42.5° while Leduc-Leballeur et al. (2020) used the 50–55° bin from the L3TB product. T_B^H and T_B^V are respectively higher and lower at low-incidence compared to Brewster angle (∼55°). Nonetheless, the principle of the melt detection algorithm is based on the large difference observed between winter and summer T_B, that is still largely valid at 40° incidence (Figure 11 gives evidence of it). It is therefore assumed that the radiometric differences between the 40° and 52.5° datasets have a negligible effect on melt detection compared to the stronger effect of the resolution enhancement.

To conclude, small adjustments were performed in the melt detection algorithm to cope with the differences in the SiER$_{40}$ and L3TB products. However, their impact is unnoticeable compared to the main effect of the resolution enhancement.

6. Conclusion

We applied the state-of-the-art rSIR image reconstruction algorithm to SMOS L1C data to produce for the first time enhanced resolution SMOS T_B maps. Three products were computed and evaluated, using the 50-55° incidence bin only (SiER$_{52.5}$), the 37.5-42.5° incidence bin only (SiER$_{40}$), and the observations with an incidence lower than 40° (MiER). The comparisons against the SMOS L3TB product show no systematic bias except for the MiER product that requires a modelisation of incidence diagrams. The spatial resolution of the SiER$_{40}$ and MiER products is estimated to around 30 km, which is a ∼30 % improvement (near 50 %, respectively) with respect to the L3TB product at 40° (52.5°).

We evaluated the impacts of this resolution enhancement for melt detection using the SiER$_{40}$ product against the L3TB at 52.5° previously used in Leduc-Leballeur et al. (2020). At global scale, there is a widespread increase of the annual average number of melt days detected in both the Greenland and Antarctic ice sheets. The largest melt enhancements (>30 days/year) are found in Greenland's percolation areas and on many Antarctic ice shelves, especially near the grounding line. We demonstrated through a case study in the Antarctic Peninsula that this gain is due to a lesser dilution of the signal produced by localized melt when the surrounding snow areas remain dry. As a consequence, an earlier and sharper increase in T_B is detected as melt in the SiER$_{40}$

product while snow status is still dry in the L3TB. The wet snow detected is also located more accurately on the ice shelves. A sharper T_{B} decrease in the SiER_{40} than in the L3TB just above the grounding lines corresponds to the only pixels with more melt days in the L3TB product.

These findings and the datasets produced are important for future studies in large-scale hydrology of the ice sheets. First, they could feed L-band and multi-frequency algorithms that aim to detect aquifers, study melt-water percolation and melt/refreeze diurnal cycles. The spatial resolution achieved in the enhanced resolution product ($\sim$30 km) is comparable for instance to AMSR2 frequency-dependent footprints ($\sim$41 km at 6.9 GHz to $\sim$8 km at 36.5 GHz), and SMOS time series extend to 2010. The enhanced resolution T_{B} maps are also a valuable input for future algorithms to estimate liquid water content. Finally, for purposes of designing the upcoming passive microwave satellite missions like ESA's Copernicus Imaging Microwave Radiometer (CIMR) and their retrieval algorithms, we demonstrated how important is the spatial resolution when coming to geophysical applications, especially in the cryosphere sciences.

Data availability

Two open access databases contain all the brightness temperature and melt maps on Greenland and Antarctica:

- `https://doi.org/10.57932/f72f9515-3699-4fae-92fc-a350075d042f` for the brightness temperature maps,
- `https://doi.org/10.57932/1970fb7c-cdb4-4ddf-9891-1e6836a46f25` for the melt maps.

Acknowledgements

This work has been funded by the Centre National d'Etudes Spatiales (CNES) grants TOSCA SMOS-TE and SMOS-HR and supported by European Space Agency's 4DGreenland project. The authors would like to thank Marion Leduc-Leballeur for her discussions and help with the melt detection algorithm.

References

Abdalati, W., & Steffen, K. (1995). Passive microwave-derived snow melt regions on the Greenland ice sheet. *Geophysical Research Letters*, *22*, 787–790.

Al Bitar, A., Mialon, A., Kerr, Y. H., Cabot, F., Richaume, P., Jacquette, E., Quesney, A., Mahmoodi, A., Tarot, S., Parrens, M. et al. (2017). The global SMOS Level 3 daily soil moisture and brightness temperature maps. *Earth System Science Data*, *9*, 293–315. doi:10.5194/essd-9-293-2017.

Ashcraft, I. S., & Long, D. G. (2006). Comparison of methods for melt detection over Greenland using active and passive microwave measurements. *International Journal of Remote Sensing*, *27*, 2469–2488. doi:doi=10.1080/01431160500534465.

Backus, G., & Gilbert, F. (1968). The resolving power of gross earth data. *Geophysical Journal International*, *16*, 169–205.

Backus, G. E., & Gilbert, J. F. (1967). Numerical applications of a formalism for geophysical inverse problems. *Geophysical Journal International*, *13*, 247–276.

Banwell, A. F., MacAyeal, D. R., & Sergienko, O. V. (2013). Breakup of the Larsen B Ice Shelf triggered by chain reaction drainage of supraglacial lakes. *Geophysical Research Letters*, *40*, 5872–5876. doi:10.1002/2013GL057694.

Banwell, A. F., Willis, I. C., Macdonald, G. J., Goodsell, B., & MacAyeal, D. R. (2019). Direct measurements of ice-shelf flexure caused by surface meltwater ponding and drainage. *Nature communications*, *10*, 730. doi:10.1038/s41467-019-08522-5.

Bell, R. E., Chu, W., Kingslake, J., Das, I., Tedesco, M., Tinto, K. J., Zappa, C. J., Frezzotti, M., Boghosian, A., & Lee, W. S. (2017). Antarctic ice shelf potentially stabilized by export of meltwater in surface river. *Nature*, *544*, 344–348. doi:10.1038/nature22048.

Bevan, S. L., Luckman, A. J., Kuipers Munneke, P., Hubbard, B., Kulessa, B., & Ashmore, D. W. (2018). Decline in surface melt duration on Larsen C ice shelf revealed by the Advanced Scatterometer (ASCAT). *Earth and Space Science*, *5*, 578–591.

Brodzik, M. J., & Long, D. G. (2018). Calibrated Passive Microwave Daily EASE-Grid 2.0 Brightness Temperature ESDR (CETB): Algorithm Theoretical Basis Document. URL: https://nsidc.org/sites/default/files/documents/technical-reference/measures_cetb_atbd_v1.pdf accessed: 7-12-2023.

Brodzik, M. J., Long, D. G., & Hardman, M. A. (2021). SMAP Radiometer Twice-Daily rSIR-enhanced EASE-Grid 2.0 Brightness Temperatures, Version 2. doi:10.5067/YAMX52BXFL10.

Colliander, A., Mousavi, M., Kimball, J. S., Miller, J. Z., & Burgin, M. (2023). Spatial and temporal differences in surface and subsurface meltwater distribution over Greenland ice sheet using multi-frequency passive microwave observations. *Remote Sensing of Environment*, *295*, 113705.

Colliander, A., Mousavi, M., Marshall, S., Samimi, S., Kimball, J. S., Miller, J. Z., Johnson, J., & Burgin, M. (2022). Ice Sheet Surface and Subsurface Melt Water Discrimination Using Multi-Frequency Microwave Radiometry. *Geophysical Research Letters*, *49*, e2021GL096599. doi:10.1029/2021GL096599.

Entekhabi, D., Njoku, E. G., O'Neill, P. E., Kellogg, K. H., Crow, W. T., Edelstein, W. N., Entin, J. K., Goodman, S. D., Jackson, T. J., Johnson, J. et al. (2010). The soil moisture active passive (SMAP) mission. *Proceedings of the IEEE*, *98*, 704–716. doi:10.1109/JPROC.2010.2043918.

ESA (2019). Algorithm Theoretical Basis Document (ATBD) for the SMOS Level 2 Soil Moisture Processor Development Continuation Project. URL: https://earth.esa.int/eogateway/documents/20142/37627/SMOS-L2-SM-ATBD.pdf accessed: 16-9-2024.

ESA (2021). SMOS Level 1 and Auxiliary Data Products Specifications. URL: https://earth.esa.int/eogateway/documents/20142/37627/SMOS-L1-Aux-Data-Product-Specification.pdf accessed: 16-9-2024.

Fettweis, X., Box, J. E., Agosta, C., Amory, C., Kittel, C., Lang, C., van As, D., Machguth, H., & Gallée, H. (2017). Reconstructions of the 1900-2015 Greenland ice sheet surface mass balance using the regional climate MAR model. *The Cryosphere*, *11*, 1015–1033. doi:10.5194/tc-11-1015-2017.

Houtz, D., Mätzler, C., Naderpour, R., Schwank, M., & Steffen, K. (2021). Quantifying surface melt and liquid water on the Greenland ice sheet using L-band radiometry. *Remote Sensing of Environment*, *256*, 112341. doi:10.1016/j.rse.2021.112341.

Imaoka, K., Kachi, M., Kasahara, M., Ito, N., Nakagawa, K., & Oki, T. (2010). Instrument performance and calibration of amsr-e and amsr2. *International archives of the photogrammetry, remote sensing and spatial information science*, *38*, 13–18.

IMBIE (2018). Mass balance of the Antarctic Ice Sheet from 1992 to 2017. *Nature*, *558*, 219–222.

IMBIE (2020). Mass balance of the Greenland Ice Sheet from 1992 to 2018. *Nature*, *579*, 233–239.

Kerr, Y. H., Waldteufel, P., Wigneron, J.-P., Delwart, S., Cabot, F., Boutin, J., Escorihuela, M.-J., Font, J., Reul, N., Gruhier, C., Juglea, S. E., Drinkwater, M. R., Hahne, A., Martín-Neira, M., & Mecklenburg, S. (2010). The smos mission: New tool for monitoring key elements ofthe global water cycle. *Proceedings of the IEEE*, *98*, 666–687. doi:10.1109/JPROC.2010.2043032.

Kerr, Y. H., Waldteufel, P., Wigneron, J.-P., Martinuzzi, J., Font, J., & Berger, M. (2001). Soil moisture retrieval from space: The Soil Moisture and Ocean Salinity (SMOS) mission. *IEEE transactions on Geoscience and remote sensing*, *39*, 1729–1735. doi:10.1109/36.942551.

Kingslake, J., Ely, J. C., Das, I., & Bell, R. E. (2017). Widespread movement of meltwater onto and across Antarctic ice shelves. *Nature*, *544*, 349–352. doi:10.1038/nature22049.

Koenig, L. S., Miège, C., Forster, R. R., & Brucker, L. (2014). Initial in situ measurements of perennial meltwater storage in the Greenland firn aquifer. *Geophysical Research Letters*, *41*, 81–85.

Kuipers Munneke, P., Luckman, A., Bevan, S., Smeets, C., Gilbert, E., Van Den Broeke, M., Wang, W., Zender, C., Hubbard, B., Ashmore, D. et al. (2018). Intense winter surface melt on an Antarctic ice shelf. *Geophysical Research Letters*, *45*, 7615–7623. doi:https://doi.org/10.1029/2018GL077899.

Leduc-Leballeur, M., Picard, G., Macelloni, G., Mialon, A., & Kerr, Y. H. (2020). Melt in Antarctica derived from Soil Moisture and Ocean Salinity (SMOS) observations at L band. *The Cryosphere*, *14*, 539–548. doi:10.5194/tc-14-539-2020.

Liang, D., Guo, H., Zhang, L., Cheng, Y., Zhu, Q., & Liu, X. (2021). Time-series snowmelt detection over the Antarctic using Sentinel-1 SAR images on Google Earth Engine. *Remote Sensing of Environment*, *256*, 112318. doi:10.1016/j.rse.2021.112318.

Liu, H., Wang, L., & Jezek, K. C. (2006). Spatiotemporal variations of snowmelt in Antarctica derived from satellite scanning multichannel microwave radiometer and Special Sensor Microwave Imager data (1978–2004). *Journal of Geophysical Research: Earth Surface*, *111*. doi:.1029/2005JF000318.

Long, D. G. (2015). An Investigation of Antenna Patterns for the CETB. URL: https://zenodo.org/records/7959217 accessed: 7-12-2023.

Long, D. G., & Brodzik, M. J. (2016). Optimum Image Formation for Spaceborne Microwave Radiometer Products. *IEEE Transactions on Geoscience and Remote Sensing*, *54*, 2763–2779. doi:10.1109/TGRS.2015.2505677.

Long, D. G., Brodzik, M. J., & Hardman, M. (2023). Evaluating the effective resolution of enhanced resolution smap brightness temperature image products. *Frontiers in Remote Sensing*, *4*, 1073765. doi:10.3389/frsen.2023.1073765.

Long, D. G., Brodzik, M. J., & Hardman, M. A. (2019). Enhanced-Resolution SMAP Brightness Temperature Image Products. *IEEE Transactions on Geoscience and Remote Sensing*, *57*, 4151–4163. doi:10.1109/TGRS.2018.2889427.

Long, D. G., & Daum, D. L. (1998). Spatial resolution enhancement of SSM/I data. *IEEE Transactions on Geoscience and Remote Sensing*, *36*, 407–417.

Luckman, A., Elvidge, A., Jansen, D., Kulessa, B., Munneke, P. K., King, J., & Barrand, N. E. (2014). Surface melt and ponding on Larsen C Ice Shelf and the impact of föhn winds. *Antarctic Science*, *26*, 625–635.

Macelloni, G., Brogioni, M., Pettinato, S., Zasso, R., Crepaz, A., Zaccaria, J., Padovan, B., & Drinkwater, M. (2013). Ground-based L-band emission measurements at Dome-C Antarctica: The DOMEX-2 experiment. *IEEE transactions on geoscience and remote sensing*, *51*, 4718–4730.

Macelloni, G., Leduc-Leballeur, M., Montomoli, F., Brogioni, M., Ritz, C., & Picard, G. (2019). On the retrieval of internal temperature of Antarctica ice sheet by using SMOS observations. *Remote Sensing of Environment*, *233*, 111405. doi:10.1016/j.rse.2019.111405.

Maezawa, H., & Miyauchi, H. (2009). Rigorous expressions for the Fresnel equations at interfaces between absorbing media. *JOSA A*, *26*, 330–336. doi:10.1364/JOSAA.26.000330.

Miège, C., Forster, R. R., Brucker, L., Koenig, L. S., Solomon, D. K., Paden, J. D., Box, J. E., Burgess, E. W., Miller, J. Z., McNerney, L. et al. (2016). Spatial extent and temporal variability of Greenland firn aquifers detected by ground and airborne radars. *Journal of Geophysical Research: Earth Surface*, *121*, 2381–2398.

Miller, J. Z., Culberg, R., Long, D. G., Shuman, C. A., Schroeder, D. M., & Brodzik, M. J. (2022). An empirical algorithm to map perennial firn aquifers and ice slabs within the Greenland Ice Sheet using satellite L-band microwave radiometry. *The Cryosphere*, *16*, 103–125.

Miller, O., Solomon, D. K., Miège, C., Koenig, L., Forster, R., Schmerr, N., Ligtenberg, S. R., Legchenko, A., Voss, C. I., Montgomery, L. et al. (2020). Hydrology of a perennial firn aquifer in Southeast Greenland: an overview driven by field data. *Water Resources Research*, *56*, e2019WR026348.

Mote, T. L. (2007). Greenland surface melt trends 1973–2007: Evidence of a large increase in 2007. *Geophysical Research Letters*, *34*.

Mouginot, J., Rignot, E., Bjørk, A. A., Van den Broeke, M., Millan, R., Morlighem, M., Noël, B., Scheuchl, B., & Wood, M. (2019). Forty-six years of Greenland ice sheet mass balance from 1972 to 2018. *Proceedings of the national academy of sciences*, *116*, 9239–9244. doi:10.1073/pnas.1904242116.

Mousavi, M., Colliander, A., Miller, J. Z., & Kimball, J. S. (2022). A Novel Approach to Map the Intensity of Surface Melting on the Antarctica Ice Sheet Using SMAP L-Band Microwave Radiometry. *IEEE Journal of Selected Topics in Applied Earth Observations and Remote Sensing*, *15*, 1724–1743. doi:10.1109/JSTARS.2022.3147430.

Nghiem, S., Hall, D., Mote, T., Tedesco, M., Albert, M., Keegan, K., Shuman, C., DiGirolamo, N., & Neumann, G. (2012). The extreme melt across the Greenland ice sheet in 2012. *Geophysical Research Letters*, *39*.

Otosaka, I. N., Horwath, M., Mottram, R., & Nowicki, S. (2023). Mass balances of the Antarctic and Greenland ice sheets monitored from space. *Surveys in Geophysics*, (pp. 1–38). doi:10.5194/essd-15-1597-2023.

Picard, G., & Fily, M. (2006). Surface melting observations in Antarctica by microwave radiometers: Correcting 26-year time series from changes in acquisition hours. *Remote Sensing of Environment*, *104*, 325–336. doi:10.1016/j.rse.2006.05.010.

Picard, G., Fily, M., & Gallée, H. (2007). Surface melting derived from microwave radiometers: a climatic indicator in Antarctica. *Annals of Glaciology*, *46*, 29–34. doi:10.3189/172756407782871684.

Picard, G., Leduc-Leballeur, M., Banwell, A. F., Brucker, L., & Macelloni, G. (2022). The sensitivity of satellite microwave observations to liquid water in the antarctic snowpack. *The Cryosphere*, *16*, 5061–5083. doi:10.5194/tc-16-5061-2022.

Piepmeier, J. R., Focardi, P., Horgan, K. A., Knuble, J., Ehsan, N., Lucey, J., Brambora, C., Brown, P. R., Hoffman, P. J., French, R. T., Mikhaylov, R. L., Kwack, E.-Y., Slimko, E. M., Dawson, D. E., Hudson, D., Peng, J., Mohammed, P. N., De Amici, G., Freedman, A. P., Medeiros, J., Sacks, F., Estep, R., Spencer, M. W., Chen, C. W., Wheeler, K. B., Edelstein, W. N., O'Neill, P. E., & Njoku, E. G. (2017). SMAP L-Band Microwave Radiometer: Instrument Design and First Year on Orbit. *IEEE Transactions on Geoscience and Remote Sensing*, *55*, 1954–1966. doi:10.1109/TGRS.2016.2631978.

Ramage, J. M., & Isacks, B. L. (2002). Determination of melt-onset and refreeze timing on southeast Alaskan icefields using SSM/I diurnal amplitude variations. *Annals of Glaciology*, *34*, 391–398.

Rignot, E., Mouginot, J., Scheuchl, B., Van Den Broeke, M., Van Wessem, M. J., & Morlighem, M. (2019). Four decades of Antarctic ice sheet mass balance from 1979–2017. *Proceedings of the National Academy of Sciences*, *116*, 1095–1103. doi:10.1073/pnas.1812883116.

Rott, H., Rack, W., Skvarca, P., & De Angelis, H. (2002). Northern Larsen ice shelf, Antarctica: Further retreat after collapse. *Annals of glaciology*, *34*, 277–282.

Rott, H., Skvarca, P., & Nagler, T. (1996). Rapid collapse of northern Larsen ice shelf, Antarctica. *Science*, *271*, 788–792.

Sahr, K., White, D., & Kimerling, A. J. (2003). Geodesic discrete global grid systems. *Cartography and Geographic Information Science*, *30*, 121–134.

Saunderson, D., Mackintosh, A., McCormack, F., Jones, R. S., & Picard, G. (2022). Surface melt on the Shackleton Ice Shelf, East Antarctica (2003–2021). *The Cryosphere*, *16*, 4553–4569.

Scambos, T., Fricker, H. A., Liu, C.-C., Bohlander, J., Fastook, J., Sargent, A., Massom, R., & Wu, A.-M. (2009). Ice shelf disintegration by plate bending and hydro-fracture: Satellite observations and model results of the 2008 Wilkins ice shelf break-ups. *Earth and Planetary Science Letters*, *280*, 51–60.

Scambos, T. A., Bohlander, J., Shuman, C. A., & Skvarca, P. (2004). Glacier acceleration and thinning after ice shelf collapse in the Larsen B embayment, Antarctica. *Geophysical Research Letters*, *31*. doi:10.1029/2004GL020670.

Scambos, T. A., Hulbe, C., Fahnestock, M., & Bohlander, J. (2000). The link between climate warming and break-up of ice shelves in the Antarctic Peninsula. *Journal of Glaciology*, *46*, 516–530. doi:10.3189/172756500781833043.

Stogryn, A. (1978). Estimates of brightness temperatures from scanning radiometer data. *IEEE Transactions on Antennas and Propagation*, *26*, 720–726.

Stokes, C. R., Sanderson, J. E., Miles, B. W., Jamieson, S. S., & Leeson, A. A. (2019). Widespread distribution of supraglacial lakes around the margin of the East Antarctic Ice Sheet. *Scientific reports*, *9*, 13823.

Tedesco, M. (2007). Snowmelt detection over the Greenland ice sheet from SSM/I brightness temperature daily variations. *Geophysical Research Letters*, *34*. doi:10.1029/2006GL028466.

Tedesco, M., & Fettweis, X. (2020). Unprecedented atmospheric conditions (1948–2019) drive the 2019 exceptional melting season over the Greenland ice sheet. *The Cryosphere*, *14*, 1209–1223. doi:10.5194/tc-14-1209-2020.

Torinesi, O., Fily, M., & Genthon, C. (2003). Variability and trends of the summer melt period of Antarctic ice margins since 1980 from microwave sensors. *Journal of Climate*, *16*, 1047–1060.

Trusel, L., Frey, K. E., & Das, S. B. (2012). Antarctic surface melting dynamics: Enhanced perspectives from radar scatterometer data. *Journal of Geophysical Research: Earth Surface*, *117*.

Wille, J. D., Favier, V., Dufour, A., Gorodetskaya, I. V., Turner, J., Agosta, C., & Codron, F. (2019). West antarctic surface melt triggered by atmospheric rivers. *Nature Geoscience*, *12*, 911–916. doi:10.1038/s41561-019-0460-1.

Williamson, A. G., Banwell, A. F., Willis, I. C., & Arnold, N. S. (2018). Dual-satellite (Sentinel-2 and Landsat 8) remote sensing of supraglacial lakes in Greenland. *The Cryosphere*, *12*, 3045–3065. doi:10.5194/tc-12-3045-2018.

Wu, L., Torres, F., Corbella, I., Duffo, N., Durán, I., Vall-llossera, M., Camps, A., Delwart, S., & Martín-Neira, M. (2013). Radiometric performance of smos full polarimetric imaging. *IEEE Geoscience and Remote Sensing Letters*, *10*, 1454–1458. doi:10.1109/LGRS.2013.2260128.

Yang, K., & Smith, L. C. (2013). Supraglacial Streams on the Greenland Ice Sheet Delineated From Combined Spectral–Shape Information in High-Resolution Satellite Imagery. *IEEE Geoscience and Remote Sensing Letters*, *10*, 801–805. doi:10.1109/LGRS.2012.2224316.

Zwally, H. J. (1977). Microwave emissivity and accumulation rate of polar firn. *Journal of Glaciology*, *18*, 195–215.

Zwally, H. J., & Fiegles, S. (1994). Extent and duration of Antarctic surface melting. *Journal of Glaciology*, *40*, 463–475.

List of Figures

1 Flowchart of the SMOS resolution-enhancement and melt detection algorithms. The output datasets are highlighted in red boxes. 6

2 Overview of the L1C flags, radiometric accuracy (RA_H) and spatial resolution variations for one SMOS snapshot on the 19th of January, 2019. **(a)** Scatterplot of the semi-minor and semi-major axes of the -3 dB antenna footprint against the incidence angle. The light blue and green curves represent all the observations. The medium blue and green curves show the remaining observations once the flagged L1C data have been discarded. The dark blue and green curves show the observations with an incidence angle <40°. **(b)** Location of the non-flagged (remaining) data and the observations with incidence angle <40° within the snapshot, and **(c)** Spatial distribution of RA_H within the snapshot with the contour of the <40° measurements in red. 7

3 Observed and modeled brightness temperatures as a function of the incidence angle over the DGG n°7144462 close to Dome C on the 19th of January, 2019 for the morning (M) and afternoon (A) passes. In **(a)** the physical multilayer model was fitted to H and V polarized T_B. **(b)** is the same for the semi-physical model that includes a linear correction term at H polarization. 8

4 Normalized T_B^V for the ideal S1 mask, SMAP rSIR-enhanced evening tracks, SMOS rSIR-enhanced multi-incidence (15-40°) and single-incidence (40°) afternoon passes and SMOS daily L3TB products over the West ice-shelf on February 7-9th, 2019 (top row) and over Anvers Island on January 25-27th, 2019 (bottom row). The red lines show the transects used to compute the effective spatial resolution of each product in Figure 5. 13

5 Estimation of the effective spatial resolution along two transects for the West ice shelf (a, b) and Anvers Island (c, d) case studies (see Figure 4 for the locations of these transects). **(a, c)** T_B plotted along the transects, **(b, d)** RMSE between the observed and convoluted images plotted against the FWHM of Gaussian kernels used for convolution. The estimated effective spatial resolutions are the FWHM at minimum RMSE for each dataset. 14

6 2010-2024 annual average number of melt days detected using SMOS rSIR-enhanced resolution dataset over Antarctica. 15

7 Difference between the 2010-2024 annual average number of melt days detected using SMOS rSIR-enhanced and SMOS L3TB datasets. A higher number of melt days in the enhanced resolution product is shown in pink. 16

8 Annual number of melt days detected over Greenland using the SMOS MiER, L3TB and the difference between both products. Fourteen melt years from 2010-2011 to 2023-2024 are presented in the panels. 17

9 Illustration of the melt onset in the Antarctic Peninsula in 2018-2019. Each map shows the number of melt days over a 4 day period for rSIR (top row) and L3TB (bottom row). Pixels A, B and C correspond to the time series in Figure 11 and P1 and P2 represent the transects shown in Figure 10. 18

10 Difference ($\Delta T_{\mathrm{B}}^{\mathrm{H}}$) between the average $T_{\mathrm{B}}^{\mathrm{H}}$ on December 27-30th, 2018 and the average winter $T_{\mathrm{B}}^{\mathrm{H}}$ computed from June 1st to August 31st, 2018, along two transects in Y (P1) and X (P2) crossing the George VI and Wilkins ice shelves. P1 and P2 are identified in Figure 9 which also shows the intensive melt occurring during the 4-day interval on both ice shelves. 19

11 Time series of $T_{\mathrm{B}}^{\mathrm{H}}$ for SMOS L3TB and SiER_{40} products from April 2018 to March 2019 for the pixels marked at locations A, B and C in Figure 6 and Figure 7 on Antarctic ice shelves. The blue (green, respectively) bars at the bottom of each subplot indicate the days where melt is detected using the SiER_{40} (L3TB). 19

Appendix A. Description of the Multi-Fresnel Thermal Emission model

The model applies to a slab of n horizontal layers $i = 1 \dots n$ with given optical depth τ_i, relative permittivity ϵ_i and temperature T_i. The model neglects scattering so that the optical depth can be calculated as the product of the layer thickness d_i and absorption coefficient κ_{ai}.

Let $J_i^{t,b}$ and $I_i^{t,b}$ be the upwelling and downwelling radiation at the top (t superscript) and bottom (b superscript) of layer i propagating with a zenith angle θ_i. The goal is to calculate the upwelling radiation emerging at the surface of the slab, in the atmosphere (formally denoted by the index $i = 0$): J_0^b. For this we formulate 1) the angles of propagation in the layers, 2) the propagation through layers, 2) the transfer through the interfaces between the layers and 3) the enforcement of the boundary conditions at the top and bottom of the slab.

Zenith angle of propagation

Applying the Snell-Descartes formula for loosly media (Maezawa & Miyauchi, 2009) to account for the refraction between the layers relates the propagation angle θ_i in every layer i to the angle in the air θ_0:

$$\mu_i = \frac{\Re\sqrt{\epsilon_i - \epsilon_0(1-\mu_0^2)}}{\Re\sqrt{\epsilon_i}} \tag{A.1}$$

where we have defined the cosine $\mu_i = \cos(\theta_i)$, and $\Re$ denotes the real part. μ_i is guaranteed to be ≤ 1 because the air is the less refractive material.

Propagation within the layers

The downwelling radiation at the bottom of layer i is the result of the downwelling radiation coming from the top of the layer and reaching the bottom with an attenuation equals to $A_k = \exp(-\tau_i/\mu)$, and by the natural thermal emission within the layer which is the product of the emissivity and temperature T_i. The emissivity is equal to the opacity of the layer, i.e. $(1 - \exp(-\tau_k/\mu))$ according to Kirchoff's law. Similarly for the upwelling radiation at the top, the propagation through the layer including the emission forms a system of two equations:

$$I_i^b = \exp(-\tau_i/\mu)I_i^t + (1 - \exp(-\tau_i/\mu))T_i \tag{A.2}$$

$$J_i^t = \exp(-\tau_i/\mu)J_i^b + (1 - \exp(-\tau_i/\mu))T_i \tag{A.3}$$

which can be written in a matrix form as follows:

$$\begin{pmatrix} I_i^t \\ J_i^t \\ 1 \end{pmatrix} = \begin{pmatrix} 1/A_i & 0 & -(1/A_i - 1)T_i \\ 0 & A_i & (1-A_i)T_i \\ 0 & 0 & 1 \end{pmatrix} \begin{pmatrix} I_i^b \\ J_i^b \\ 1 \end{pmatrix} \tag{A.4}$$

with the radiation at the top of the layer on the left and the bottom on the right.

Propagation through the interfaces

For each interface, the upwelling and the downwelling radiation can be written as the sum of the reflected and the transmitted radiation, leading to the two following equations:

$$J^b_{i-1} = r_i I^b_{i-1} + t'_i J^t_i \tag{A.5}$$

$$I^t_i = t_i I^b_{i-1} + r'_k J^t_i \tag{A.6}$$

where r_i and t_i are the reflection and transmission coefficient from layer $i-1$ to layer i, and r'_i and t'_i from layer i to layer $i-1$. Given that the propagation angles in adjacent layers are related through Snell-Descarte's law, $r'_i = r_i$ and $t'_i = t_i$, and by energy conservation $t_i = 1 - r_i$. Written in matrix form this yields:

$$\begin{pmatrix} I^b_{i-1} \\ J^b_{i-1} \\ 1 \end{pmatrix} = \frac{1}{1-r_i} \begin{pmatrix} 1 & -r_i & 0 \\ r_i & 1-2r_i & 0 \\ 0 & 0 & 1-r_k \end{pmatrix} \begin{pmatrix} I^t_k \\ J^t_k \\ 1 \end{pmatrix} \tag{A.7}$$

Combined transfer matrix

Combining Equations A.4 and A.7 provides the transfer matrix M_i which links the radiance at the bottom of two successive layers:

$$M_i = \frac{1}{1-r_1} \begin{pmatrix} P_i & -r_i P_i & \left(-(1/P_i - 1) - r_i(1-P_i)\right) T_i \\ r_i/P_i & (1-2r_i)P_i & \left(-r_i(1/P_i - 1) + (1-2r_i)(1-P_i)\right) T_i \\ 0 & 0 & 1-r_i \end{pmatrix}. \tag{A.8}$$

To represent the substrate at the bottom of the slab (characterized by its reflection coefficient r_{sub} and temperature T_{sub}) , it is possible to add a semi-infinite layer with the transfer matrix M_{n+1} given by Eq A.8 where $r_{n+1} = r_{\text{sub}}$ and $T_= T_{\text{sub}}$ and $P_{n+1} = 0$.

Then, combining the transfer matrices for each layer and the substrate leads to:

$$\begin{pmatrix} I^b_0 = 0 \\ J^b_0 \\ 1 \end{pmatrix} = \prod_{i=1}^{n+1} M_i \begin{pmatrix} I^b_n \\ J^b_n = 0 \\ 1 \end{pmatrix} \tag{A.9}$$

where the downwelling radiation coming from the atmosphere at the top of the slab is $I^b_0 = 0$ and the upwelling radiation coming from the bottom of the infinite layer representing the substrate is $J^b_{n+1} = 0$.

Emerging radiation

Equation A.9 provides two linear equations with two unknowns J_0^b and I_n^b, which is solved to yield the emerging radiation at the top of the slab as follows:

$$J_0^b = (-m_{21}m_{13}/m_{11} + m_{23})/m_{33} \tag{A.10}$$

where m_{jk} are the elements of the matrix $\prod_{i=1}^{n+1} M_i$. This solves the problem.